AIAA Journal, Available online 13 November 2024
DOI: 10.2514/1.j064521

# Shock-induced Fan Cowl Separation during Aeroengine Windmilling at Diversion from Cruise[*]

Kshitij Sabnis[†]
*School of Engineering and Materials Science, Queen Mary University of London, London, E1 4NS, UK*
*Department of Engineering, University of Cambridge, Cambridge, CB2 1PZ, UK*

Holger Babinsky[‡]
*Department of Engineering, University of Cambridge, Cambridge, CB2 1PZ, UK*

Luca Boscagli[□] and David MacManus[¶]
*Centre for Propulsion Engineering, Cranfield University, Cranfield, MK43 0AL, UK*

Christopher Sheaf[‖]
*Installation Aerodynamics, Rolls–Royce plc, Derby, DE24 8BJ, UK*

**When a civil aircraft engine is operated at windmill during the cruise flight phase, there is supersonic flow acceleration around the leading edge of the fan cowl towards the external surface. The terminating normal shock wave can separate the turbulent boundary layer developing on this external surface. A series of experiments at flight-relevant Reynolds number (1.2 million based on lip thickness) are performed in a quasi-two-dimensional wind tunnel rig to investigate the underlying flow physics. At nominal inflow Mach number of 0.65 and nacelle incidence angle of 4.5 degrees, as the equivalent engine mass-flow rate is reduced, an increase in shock strength results in flow separation when the shock exceeds Mach 1.4. Over a 10% range in notional engine mass-flow rate, the boundary layer developing on the external fan cowl thickens by a factor of three on the onset of separation. A reduction in incoming Mach number from 0.65 to 0.60 weakens the shock wave and thus delays separation. An increase in surface roughness has no significant effect in situations where the boundary layer remains attached. However, for separated cases, an increased local roughness height causes a greater separation extent and a thicker boundary layer downstream of the shock wave.**

---

[*] Presented as Paper 2023-3394 at the AIAA Aviation 2023 Forum, San Diego, CA, 12–16 June 2023.

[†] Lecturer in Aerospace Engineering, School of Engineering and Materials Science, Queen Mary University of London, AIAA Member. A significant portion of the research was conducted when the author was a Research Associate at the University of Cambridge. Corresponding author: k.sabnis@qmul.ac.uk

[‡] Professor of Aerodynamics, Department of Engineering, University of Cambridge, AIAA Fellow.

[□] Research Fellow, Centre for Propulsion Engineering, Cranfield University.

[¶] Professor of Propulsion Aerodynamics, Centre for Propulsion Engineering, Cranfield University.

[‖] Installation Aerodynamics Specialist, Installation Aerodynamics, Rolls–Royce plc.

# Nomenclature

$A$, $B$ = Stern–Volmer coefficients

$h_b$ = height of bump

$H_i$ = incompressible shape factor

$I$ = light intensity from pressure-sensitive paint

$L$ = length

$M$ = Mach number

$p$ = pressure

$R$ = surface roughness height

Re = Reynolds number

$s$ = chord-wise coordinate from lip highlight

$T$ = temperature

$U$ = velocity vector magnitude

$x$ = streamwise coordinate from tunnel entry

$y$ = vertical coordinate from tunnel upper wall

$y_w$ = local wall-normal coordinate

$\Delta y$ = tunnel height

$z$ = spanwise coordinate

$\delta$ = physical boundary-layer thickness

$\delta_i^*$ = incompressible displacement thickness

$\kappa$ = surface curvature

$\theta_i$ = incompressible momentum thickness

Subscripts

in = inflow quantity

ise = isentropic quantity

max = maximum value

nac = quantity relating to nacelle model

ref = quantity relating to reference condition

0 = stagnation quantity

$\infty$ = free-stream quantity

Superscripts

$+$ = wall units

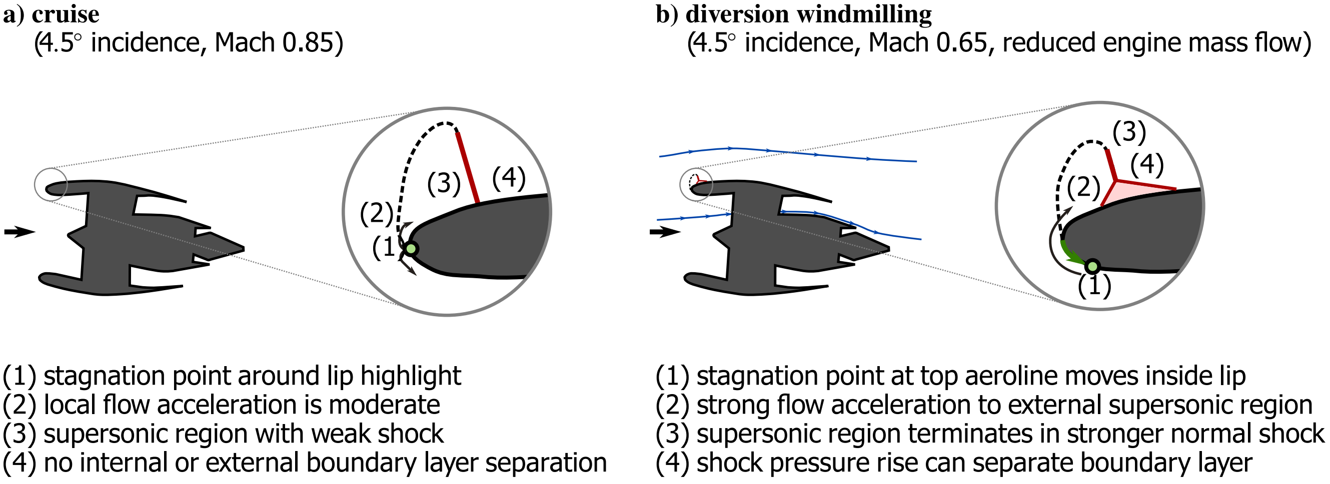

**Fig. 1 Schematic of flow fields for (a) on-design cruise and (b) off-design diversion windmilling conditions.**

# I. Introduction

Engine nacelles for civil aircraft are typically optimised for aerodynamic efficiency under design conditions such as cruise. The aerodynamic behaviour is generally well understood at these design points, where the optimised fan cowl geometries do not exhibit any significant flow separation on the internal or external nacelle surfaces [1]. However, the flow field in off-design scenarios, such as engine windmilling, has not been studied extensively and the detailed aerodynamics remains relatively unknown. For high-bypass ratio (HBPR) engines currently in service, these off-design scenarios are typically not problematic because sufficient design margins ensure that significant flow separation is avoided [2].

However, such an approach is generally not possible for ultra high-bypass ratio (UHBPR) engines, which the aviation industry is actively developing to satisfy environmental targets such as the European Commission's FlightPath 2050 vision [3]. Since UHBPR engines feature significantly larger fans than existing HBPR models, it is necessary to minimise the drag penalty from the wetted area of the fan cowl by developing more compact nacelles. These geometries may feature higher local curvature at the lip, and are thus more prone to flow separation in off-design scenarios [4]. As a result, it is not possible to maintain the same design margins used for existing HBPR engines, and so greater insight into the onset of flow separation at off-design conditions is required.

An off-design scenario particularly relevant to UHBPR engine nacelles concerns windmilling during diversion conditions in the cruise phase. In this situation, termed "diversion windmilling", the mass-flow rate through the engine is decreased and the aircraft cruise Mach number is reduced. Within the context of the present work, nominal diversion conditions for long-range aircraft are defined by a nacelle incidence angle of 4.5 degrees and an incoming Mach number of 0.65 [5]. Under diversion windmilling conditions, the reduced engine mass-flow rate results in a contracted capture streamtube and thus the stagnation point moves inside the nacelle lip (Fig. 1). As a result, the flow acceleration around the highly-curved lip causes a local supersonic region to form on the outside of the nacelle and the terminating normal shock wave can become strong enough to separate the external fan-cowl boundary layer [6]. This local flow separation can increase drag, which is undesirable under the reduced thrust conditions caused by the inoperative engine [7]. The boundary-layer separation can also result in adverse interactions with the wing flow field [6], which is especially relevant for UHBPR engine configurations which are typically installed close to the wing.

It is worth noting that similar shock/boundary-layer interactions around nacelles also occur on the inner intake surface during high-incidence take off [8] or during crosswind conditions [9]. In both these cases, the aerodynamics of the lip, where the shock tends to be located, are closely coupled to the flow further downstream in the diffuser. As a result, any local shock-induced separation tends to be associated with a change in operating conditions, including the possibility of an open boundary-layer separation under the notable adverse pressure gradient in the diffuser [10]. Whilst such interdependence is slightly reduced during high-incidence conditions by the radial mass flow redistribution due to the fan in short UHBPR intakes [8], crosswind conditions which feature ingestion of a ground vortex typically display significant unsteady coupling between the shock and the fan [9]. Thus, for the internal flow of an intake, the design of the lip and of the diffuser need to be considered simultaneously [11]. On the other hand, the windmilling aerodynamics of the forebody and the afterbody on the external fan cowl surface can be considered to be relatively independent. For example, under diversion windmilling the post-shock boundary layer reaches a quasi-equilibrium state, with a constant ratio of pressure to shear forces [12]. This situation is quite different to the internal intake behaviour during high incidence or crosswind, and so a targeted investigation of the diversion windmilling flow field is required.

The development of novel compact UHBPR nacelles requires greater understanding of the physical mechanisms governing shock-induced separation during diversion windmilling. In addition, whilst Reynolds-averaged Navier–Stokes (RANS) methods are typically used in industry to compute such flow fields [13], the capabilities of these methods to reliably predict the onset of flow detachment, the scale of separation, and the effect on the external fan cowl boundary layer remain unknown. In particular, RANS methods based on linear eddy-viscosity turbulence models can accurately compute the flow field where the boundary layer remains attached but, when flow separation occurs, such approaches cannot reliably capture the shock characteristics, the streamwise separation extent and the post-shock boundary-layer profile [12]. Often, RANS computations tend to predict a lower-momentum boundary-layer profile compared to experiment, which may be due to difficulties in capturing the boundary-layer response to the shock [12]. Thus, by conducting detailed experiments in areas where RANS methods encounter difficulties, we aim to provide data which can be compared with computational fluid dynamics (CFD) methods to identify physical separation mechanisms and characteristics of the boundary-layer response to the shock. There are also aspects where RANS capabilities remain unknown, such as the effects of surface roughness on boundary-layer development, which new experiments can help determine.

In order to increase understanding of the complex flow physics pertinent to windmilling for UHBPR fan cowls, experiments are performed in a quasi-two-dimensional (quasi-2D) transonic test rig which was developed to replicate the external aerodynamics from a full-scale three-dimensional (3D) nacelle. The current paper considers a nominal diversion windmilling condition with mass-flow capture ratio (MFCR) roughly 30 – 40% lower than cruise. The aerodynamic behaviour for three different "windmilling severities" corresponding to different MFCR values is assessed, such that the test cases encompass attached and separated nacelle conditions. The effects of incoming Mach number and surface roughness on the external fan cowl surface are also investigated.

## II. Research Methodology

### A. Wind tunnel rig

The experimental rig used in the current study is installed into a blow-down transonic wind tunnel at the University of Cambridge. The facility, schematically depicted in Fig. 2a, is driven from a high-pressure reservoir through a settling chamber, where it passes through a number of flow straighteners and turbulence grids. The flow then enters a 18:1 area ratio contraction with a round-to-rectangular transition before reaching the test section shown in Figs. 2b and 2c. The stagnation pressure is set at $204 \pm 1$ kPa and the stagnation temperature is measured to be $302 \pm 5$ K. The test section, which is 114 mm wide and 1200 mm long, consists of an underlying support structure, marked in light gray in Fig. 2b, onto which custom-built liner blocks (dark gray) are installed. The sidewalls of the wind tunnel are formed by removable doors containing an optical-access window with 203 mm diameter, which is centred at $x = 225$ mm and $y = 150$ mm, using the coordinate systems defined in Fig. 2.

The detailed design of the rig shown in Fig. 2b is set out in Refs. [14] and [15] with a brief summary included here for completeness. A 1/14th scale model of a nacelle of length, $L_{nac} = 407$ mm, is installed within the flow path, suspended from the upper wall by plates on each sidewall (Fig. 2c). These nacelle-holding plates are about 6 mm wide (5% of the tunnel width) and are chamfered at the leading and trailing edges.

The surface-streamwise coordinate, $s$, is defined from the nacelle lip highlight. This nacelle model is based on a representative 3D non-axisymmetric baseline nacelle for a long-range aircraft, which is optimised for drag whilst ensuring acceptable aerodynamic performance in a number of off-design conditions including diversion windmilling [16]. The geometry of the wind tunnel model is equivalent to the side aeroline from this full-scale 3D design. Due to structural constraints, the model is installed in an inverted configuration such that the lower surface corresponds to the external fan cowl and the upper surface is internal to the nacelle. The model consists of an additively-manufactured resin sleeve which fits onto a steel core that provides structural rigidity.

The geometry of the test section walls are based on a planar slice through 3D RANS computations of the full-scale nacelle under diversion windmilling conditions. This approach neglects curvature effects associated with the azimuthal pressure gradient imposed on the boundary layer in a 3D nacelle. It is likely that this assumption is valid because the geometric curvature in the spanwise direction is an order of magnitude smaller than the streamwise curvature. Indeed,

**a) wind tunnel infrastructure**

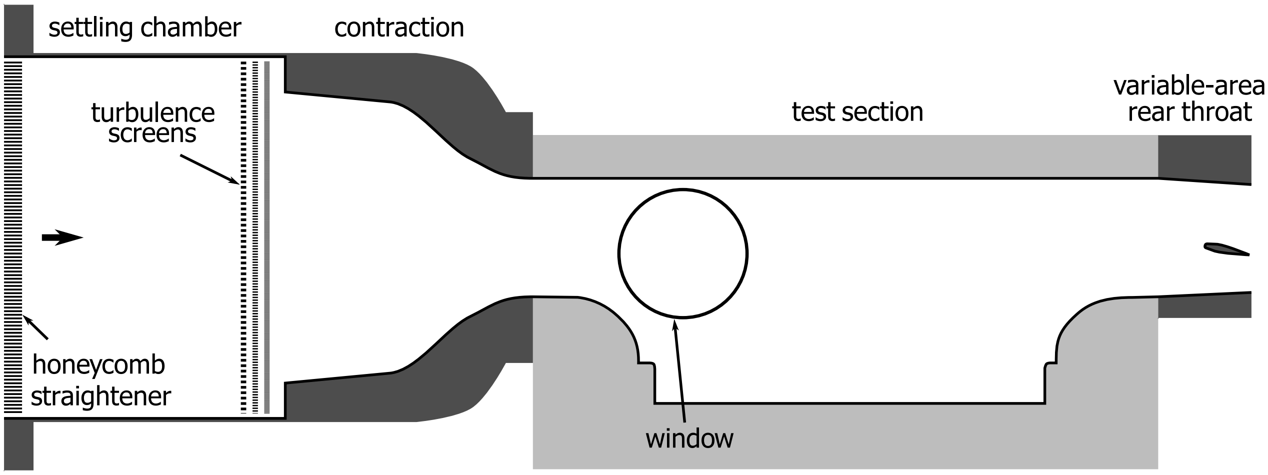

**b) test section set up**

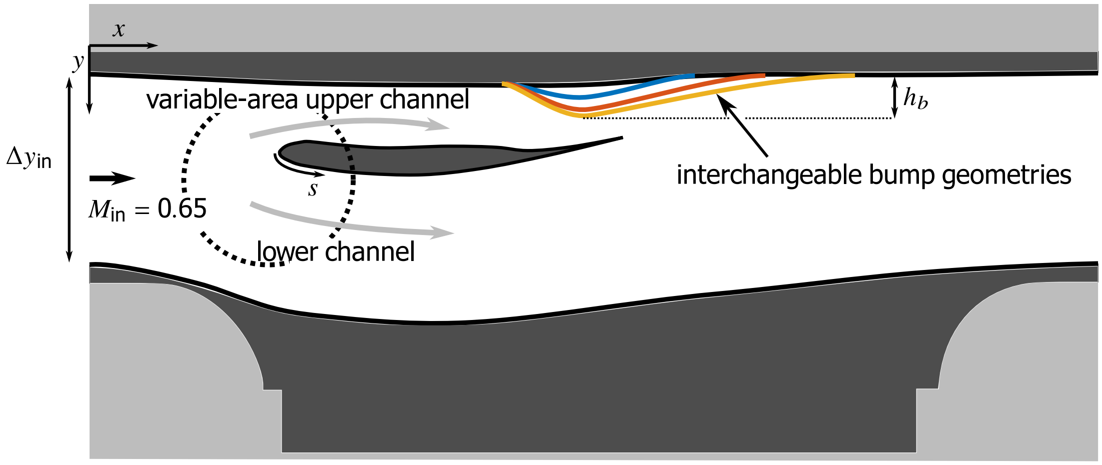

**c) photograph of installed rig**

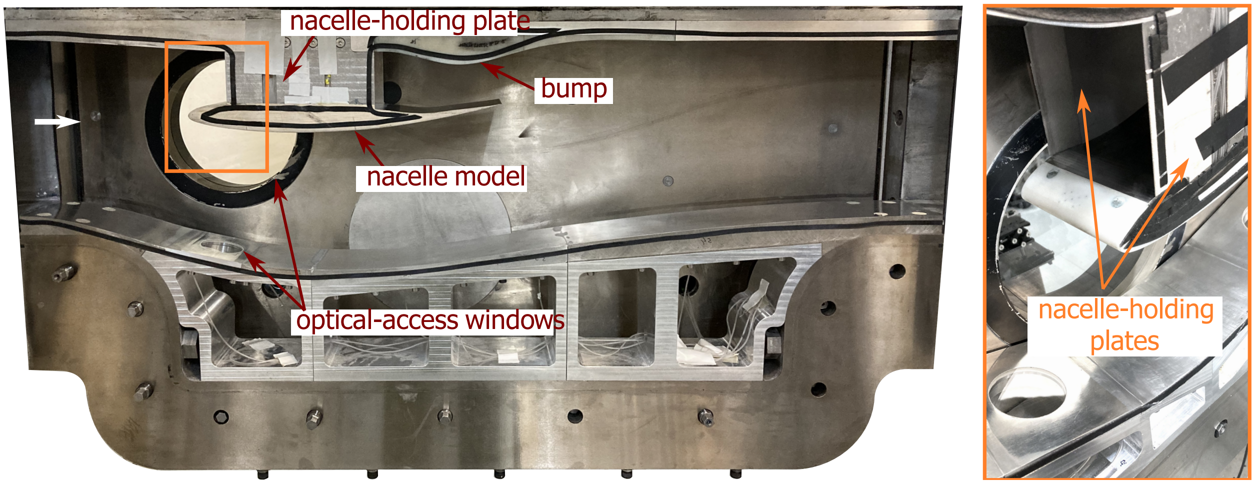

**Fig. 2** a) Schematic of the wind tunnel facility; b) detail of test section; c) photograph of installed rig.

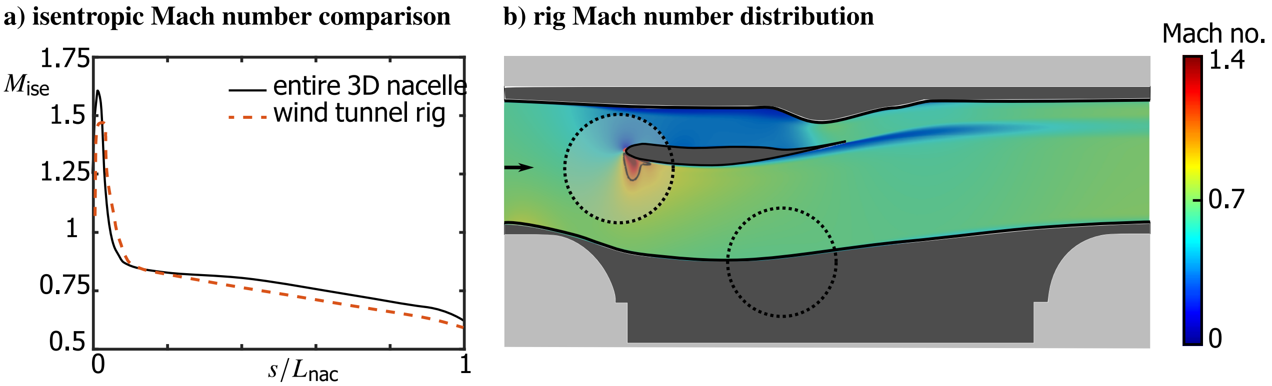
a) isentropic Mach number comparison

b) rig Mach number distribution

**Fig. 3 a) Isentropic Mach number distribution on external surface for full-scale 3D nacelle and test rig (strong windmilling). b) Centreline Mach number distribution for the test rig geometry (strong windmilling).**

computations of the 3D nacelle indicate that the boundary layer ahead of the shock wave is not subject to significant cross flow [15]. It is therefore expected that the quasi-2D rig adequately captures the key physical mechanisms governing shock-induced separation in practical applications, with further 3D-nacelle wind tunnel tests required to quantify the effects of curvature and cross flow, which are outside the scope of the present study.

The contour of the upper tunnel liner wall in Fig. 2b is defined by a streamline internal to the aircraft engine from the planar slice through 3D nacelle computations. The geometry of the lower wall in Fig. 2b is determined using a parametric design approach which uses RANS computations of the wind tunnel flow path to achieve a flow field that is representative of the full-scale 3D nacelle. Specifically, the lower wall contour is chosen such that the pressure distribution imposed on the nacelle model matches the equivalent values on the external fan cowl surface of a three-dimensional nacelle during diversion windmilling, as shown in Fig. 3 [15]. By using RANS computations of the wind tunnel flow path in the design process, the final rig geometry accounts for the prismatic nature of the set up, the boundary layers developing on the wind tunnel walls, and additional blockage associated with the nacelle-holding plates. The tunnel walls are sufficiently far away from the nacelle model that they are not expected to influence the flow on the external fan cowl surface under the conditions investigated in the current study.

Despite the 1/14th physical scale of the nacelle model, the fact that the facility is pressurised means that the Reynolds number based on lip thickness ($1.2 \times 10^6$) is only a factor of three lower than the full-scale value ($3.7 \times 10^6$). Nevertheless, whilst the shock–boundary-layer interaction (SBLI) for the full-scale nacelle is expected to be turbulent [15], infrared thermography measurements of the external fan cowl surface in the rig feature a temperature distribution at the normal shock wave characteristic of a laminar interaction [17]. Therefore, in order to replicate the turbulent interaction, the wind tunnel model is modified to promote transition by increasing the surface roughness in a small region around the leading edge between $s/L_{\text{nac}} = -0.043$ on the internal surface and $s/L_{\text{nac}} = 0.013$ on the external surface. After the local surface roughness height in this small region is increased from 2.1 microns to 15.5 microns, the temperature distribution is measured to be typical of a turbulent interaction [17].

It is desirable to reproduce the effect of different engine mass-flow rates within the rig, which correspond to different degrees of "windmilling severity". This is achieved by noting that the nacelle model splits the wind tunnel into two channels, where the upper channel corresponds to flow internal to the engine and the lower channel represents the external flow. Therefore, variations in engine mass-flow rate are replicated by adjusting the mass-flow split between these two channels. To do so, the upper wall is modified by installing a series of interchangeable variable-height bumps, shown in Fig. 2. These bumps restrict the flow through the upper channel, thus modifying the mass-flow split between the two channels. In this study, three mass-flow split cases are considered with values of bump height normalised by test-section entry height $h_b/\Delta y = 0.159$, 0.194 and 0.227. These effective engine mass flow rates, which are termed "mild", "moderate" and "strong" windmilling, respectively, represent a roughly 10% range in MFCR values around the expected onset of external fan cowl boundary-layer separation [12, 14]. Within the wind tunnel rig, the mass flow split changes from approximately 25% through the upper channel (and 75% through the lower channel) for mild windmilling, to 20% through the upper channel for strong windmilling.

There is an adjustable "rear throat" downstream of the test section (Fig. 2a). The choking of the flow at this location is achieved by an airfoil which can be adjusted to set the effective local flow area. The effective area ratio between this rear throat and the entry to the test section defines the tunnel entry Mach number. The current study considers two entry Mach numbers, the nominal value for a diversion windmilling scenario, $M_\infty = 0.650 \pm 0.002$ and a reduced value of $M_\infty = 0.600 \pm 0.002$.

As well as considering variations in effective engine mass-flow rate and inflow Mach number, the current paper also investigates the effect of surface roughness on the external fan cowl surface. The local surface roughness height, $k$, is measured using a Taylor Hobson Form Talysurf I-129 profilometer to a resolution of 8 nm. As already discussed, the local surface roughness height is 15.5 microns between $s/L_{\text{nac}} = -0.043$ and $s/L_{\text{nac}} = 0.013$, in order to promote boundary-layer transition and replicate the turbulent shock–boundary-layer interaction which features in industrial settings. The surface roughness height on the internal nacelle surface between $s/L_{\text{nac}} = -0.043$ and the trailing edge is measured to be 2.0 microns. On the external nacelle surface, two different cases are investigated: a "smooth" case with a surface roughness height of 2.0 microns and a "rough" case with a surface roughness height of 16.1 microns. The smooth and rough cases therefore correspond to roughness Reynolds numbers, $Re_k = 72$ and 560, respectively, which represent roughness heights of 6 microns and 50 microns at full scale.

### B. Experimental techniques

A z-type schlieren system with a horizontal knife-edge enables visualisation of spanwise-averaged density gradients. Schlieren images are captured at 6400 frames per second using a Photron Fastcam Nova S6 camera, with an exposure time of $1.6\ \mu$s. Time-averaged images presented in the current paper represent mean pixel intensities over 1800 consecutive frames.

Steady-state surface pressure distributions are measured using pressure-sensitive paint (PSP). The surface of interest is sprayed with a special polymer binder seeded with luminescent molecules. When irradiated by UV light, the resultant luminescence intensity ratio ($I_{\text{ref}}/I(p,T)$) is dependent on the local pressure, as specified by the Stern–Volmer relation [18]:

$$\frac{I_{\text{ref}}}{I(p,T)} = A(T) + B(T)\frac{p}{p_{\text{ref}}} \tag{1}$$

The luminescence is recorded using a RaspberryPi camera module 3 with a Sony IMX708 sensor. This camera module is installed within the tunnel rig and optical access to the model is provided through a custom optical-access window integrated into the lower liner (Fig. 2c). The reference condition is taken with the wind tunnel off, such that $p_{\text{ref}} = 101$ kPa everywhere. In order to determine the values of $A(T)$ and $B(T)$ in the Stern–Volmer relation, in-situ calibration is performed using at least ten 0.3 mm diameter static pressure taps connected to a differential pressure transducer. The location of these static pressure taps is accurate to within $\Delta x = 0.0008L_{\text{nac}}$. The overall measurement uncertainty for static pressure values using the tap data is 1% [19]. This error bound on pressure measurements corresponds to an uncertainty in the isentropic Mach number $\Delta M_{\text{ise}} = 0.01$ on the external fan cowl surface and $\Delta M_{\text{ise}} = 0.07$ around the stagnation point (where $M_{\text{ise}}$ is very sensitive to $p/p_0$).

The calibration enables absolute pressure values on the target surface to be extracted from the measured light intensity. A comparison between static tap pressures and the calibrated PSP data places an uncertainty bound of 5% on these measurements. However, in regions where the thermal properties change (e.g. attachment screws or thickness variations in the underlying steel structure) or where reflections from the tunnel walls distort the measured luminescence, the calibration is no longer valid. Due to the larger, unquantified error in such locations, the PSP data away from the tunnel centre line is used only to provide a qualitative representation of the surface pressure field.

The topology of the separated flow field is surveyed using the time-averaged skin-friction lines from surface oil-flow visualisation. This technique involves coating the surface of interest with a mixture made from paraffin, finely-powdered titanium dioxide, oleic acid and lubricating oil. There is a small error due to oil-flow producing an inaccurate indication of separation location, by about 0.2 local boundary-layer thicknesses = 0.6 mm [20]. Nevertheless, oil-flow visualisation allows the flow topology to be determined and comparisons of separation size between different setups are considered to be reliable.

Point measurements of local flow velocity are provided by two-component laser Doppler velocimetry (LDV). The flow is seeded with paraffin in the settling chamber; previous measurements of particle lag through a normal shock have placed the seeding droplet diameter in the range $200-500$ nm [19]. The error in measured velocities due to the finite number density of seeding particles and due to the laser optics is 2% for the majority of measurement points through the boundary layer, although it does increase to approximately 20% in the immediate vicinity (within 0.5 mm) of the wall as a result of laser light scattering from the model surface. In practice, LDV is not precisely a point-measurement technique, since velocities are averaged over a nominal ellipsoidal probe volume which spans 0.1 mm in the streamwise and vertical directions, and 2 mm in the spanwise direction. The positional accuracy of this probe volume is, approximately, $\Delta x \approx 0.2$ mm, $\Delta y_w \approx 0.005$ mm, and $\Delta z \approx 0.1$ mm.

Boundary-layer traverses are carried out with wall-normal resolution roughly 0.1 mm. The measured boundary-layer data is fitted to theoretical profiles. A Sun & Childs (1973) fit [21], adapted to include a van Driest compressibility correction, is used for the outer layer; this combines a log-law of the wall region with a Coles wake function. The viscous sublayer is modelled using a Musker (1979) fit [22]. These fitted profiles are then used to calculate characteristic boundary-layer integral parameters: displacement thickness ($\delta_i^*$), momentum thickness ($\theta_i$) and shape factor ($H_i$). The boundary-layer properties are determined in their incompressible forms, as these are less sensitive to variations in Mach number and require fewer assumptions to calculate from raw velocity data [23]. Whilst the theoretical profiles were originally derived for equilibrium boundary layers, the method of using parametric fitted profiles to obtain integral parameters has been shown to be robust even for non-equilibrium boundary layers, up to a shape factor of 2.8 [24]. Such an approach avoids errors caused by poor measurement resolution near the wall and therefore provides a more accurate estimate of integral boundary-layer parameters. The LDV data obtained in this study typically has around 40 measurement points within the boundary layer and the closest data point to the wall is at around $y^+ = 80$. This corresponds to an uncertainty in integral parameters of around 5% for the turbulent boundary layers measured in this study ($1.4 < H_i < 2.2$) [24].

## III. Results & Discussion

### A. Effect of engine mass flow rate

The effect of variations in equivalent engine mass-flow rate is studied for nominal diversion windmilling conditions, i.e. $M_\infty = 0.65$, and a smooth external fan cowl surface. The severity of the windmilling scenario is increased (from mild to moderate to strong) by installing bumps with larger height on the upper wall, thus replicating the reduction in engine MFCR. Schlieren images for all three windmilling severities are presented in Fig. 4. Note that, although the nacelle model has been inverted in the rig to enable better integration with the existing structure, these schlieren images have been returned to the conventional orientation (with the external fan cowl surface at the top) for convenience. The images all contain a dark region immediately upstream of the leading edge, which is related to the optical distortion caused by the strong local acceleration. The supersonic region can be visualised by the presence of weak pressure waves emanating from the surface. The terminating normal shock appears in the schlieren images as a dark line approximately normal to the external fan cowl surface. The boundary layer downstream of the shock can be identified as a bright region which grows along the external nacelle surface.

As the "windmilling severity" is increased (equivalent to a reduction in MFCR), the supersonic region grows in size

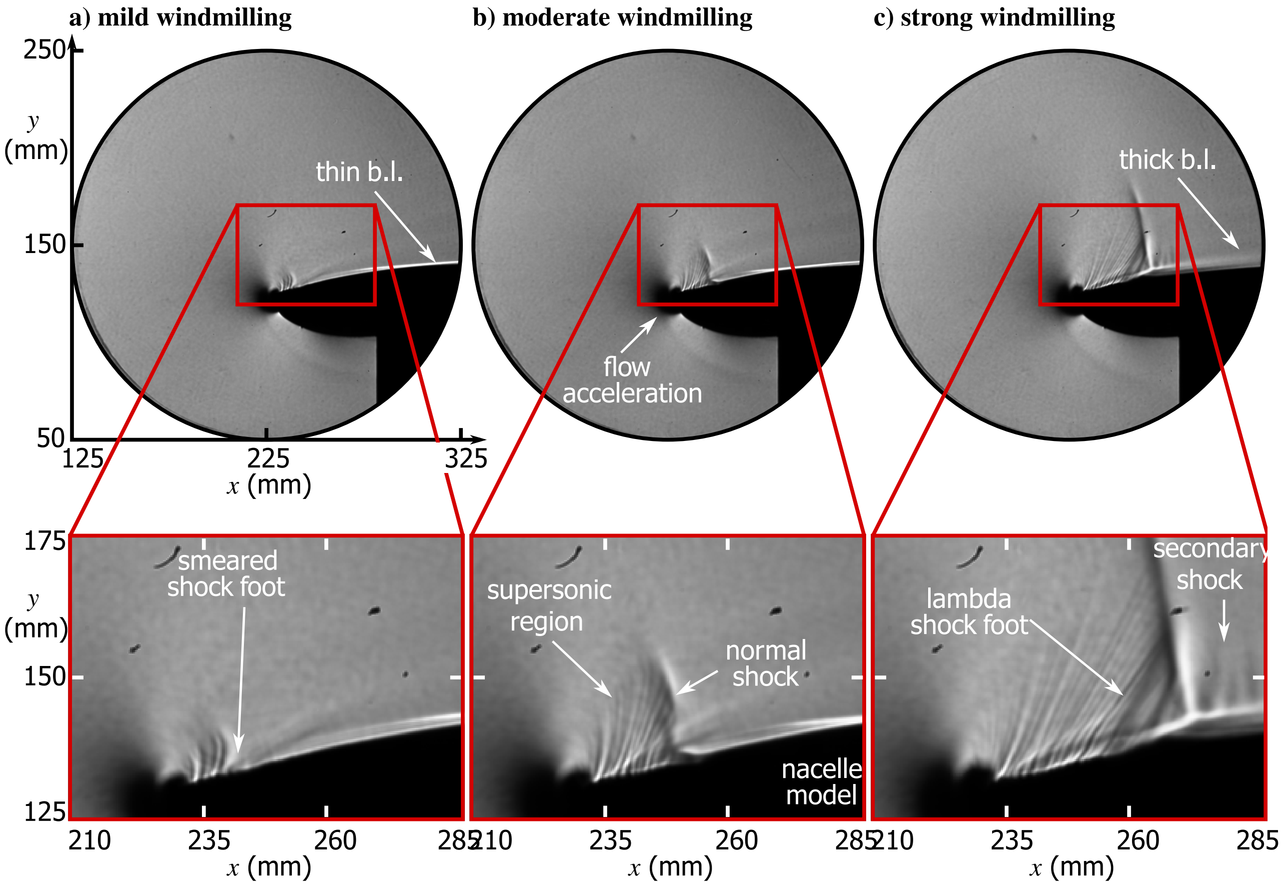

Fig. 4 Schlieren visualisation for a smooth surface at Mach 0.65.

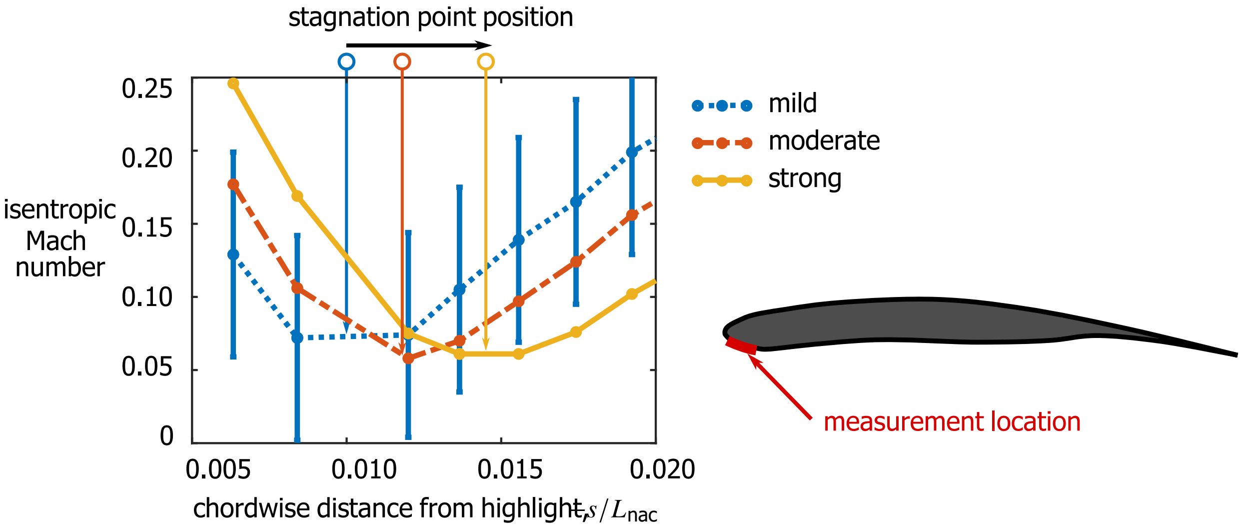

Fig. 5 Isentropic Mach number around the stagnation point for a smooth surface at Mach 0.65. Error bars for the other data sets are excluded for clarity but are consistent with the mild windmilling case.

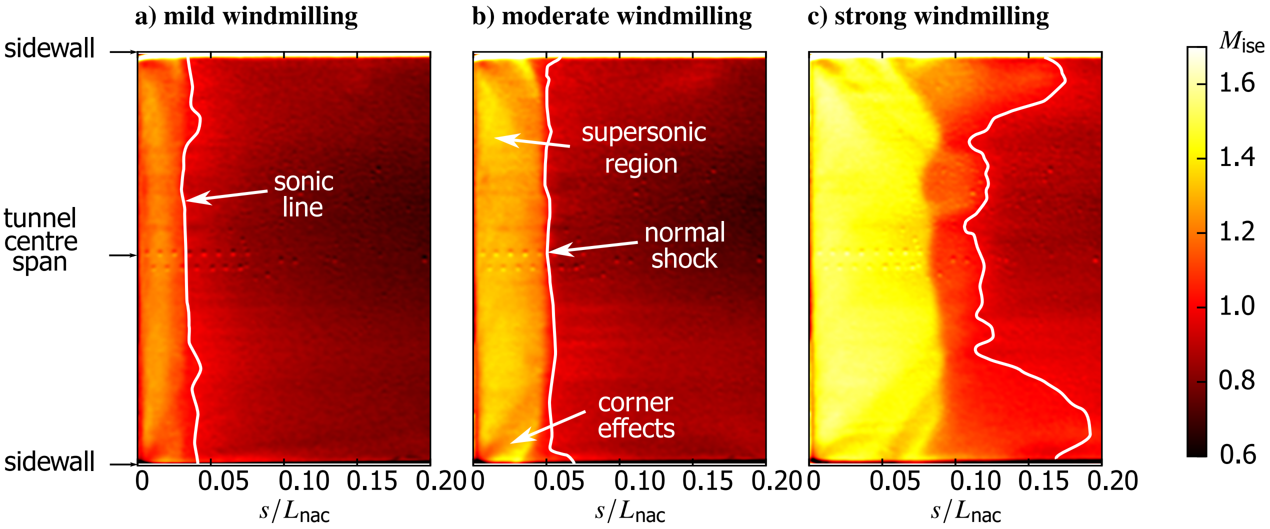

**Fig. 6** **Isentropic Mach number distribution from PSP on the external surface for a smooth surface at Mach 0.65.**

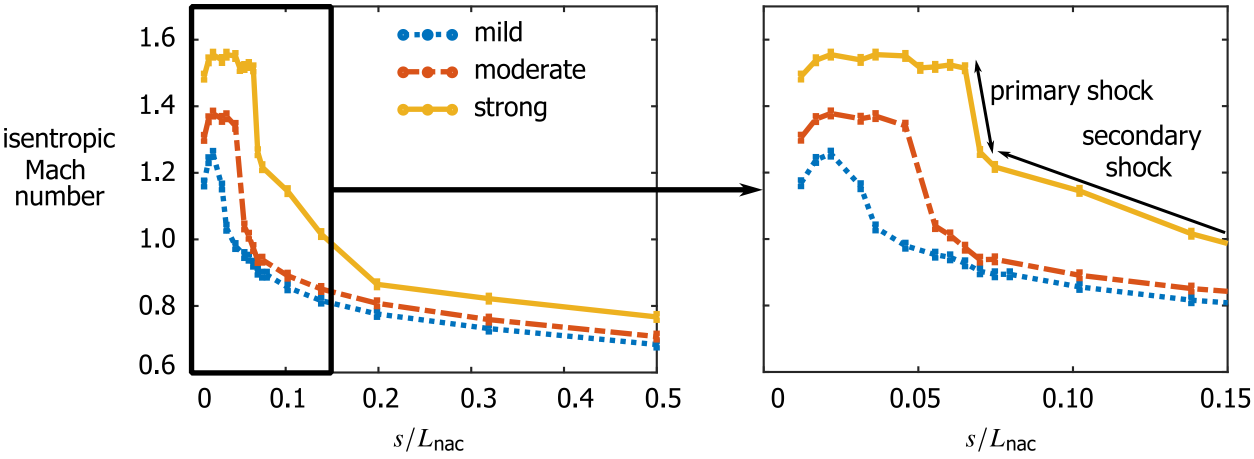

**Fig. 7** **Isentropic Mach number on the centre span of the external surface for a smooth surface at Mach 0.65.**

as the normal shock moves downstream. The SBLI structure also progresses from an attached interaction with a smeared shock foot in Fig. 4a to a lambda-shock structure typical of a separated SBLI in Fig. 4c. The downstream boundary layer accordingly becomes thicker as the windmilling severity is increased. In addition, the strong windmilling flow field (Fig. 4c) contains a secondary shock due to local re-acceleration of the post-shock subsonic flow to a supersonic condition.

The observed differences in shock-wave structure and boundary-layer response are related to the pressure distribution around the stagnation point on the internal surface, presented in Fig. 5. The profiles show a minimum at about $M_{ise} = 0.05$, which appears to be significantly different to the stagnation condition ($M_{ise} = 0$). This discrepancy is related to measurement uncertainty, with the stagnation condition ($M_{ise} = 0$) lying inside the stated error bounds ($\Delta M_{ise} = 0.07$) of the measured minimum value ($M_{ise} = 0.05$). Furthermore, whilst the error bars in Fig. 5 may

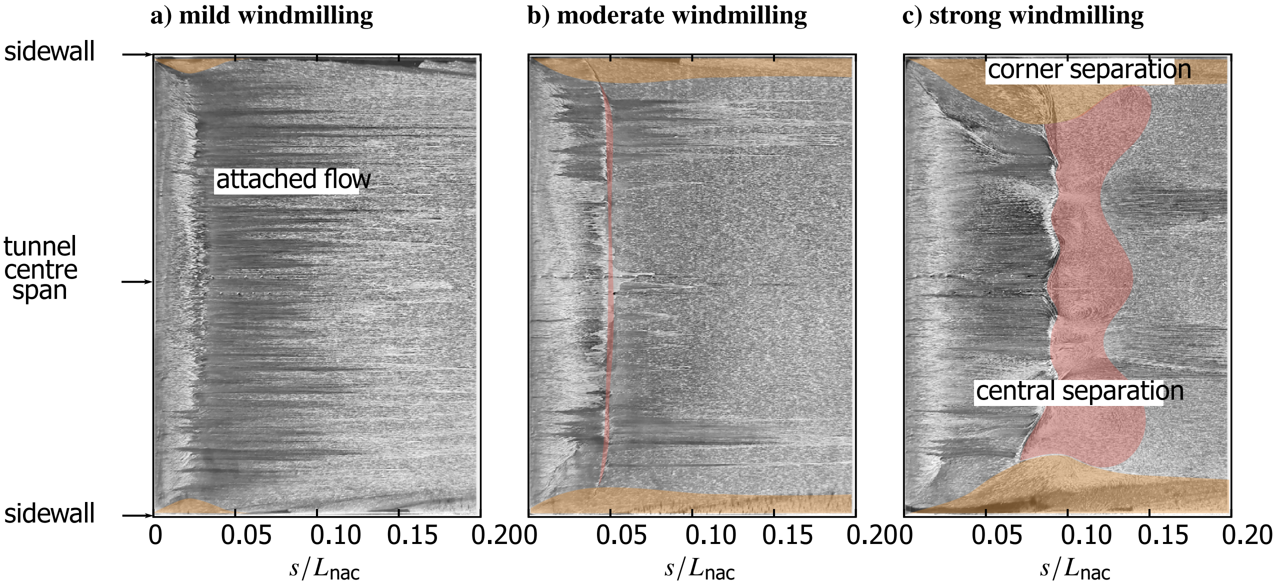

**Fig. 8** Surface oil-flow visualisation on the external surface for a smooth surface at Mach 0.65.

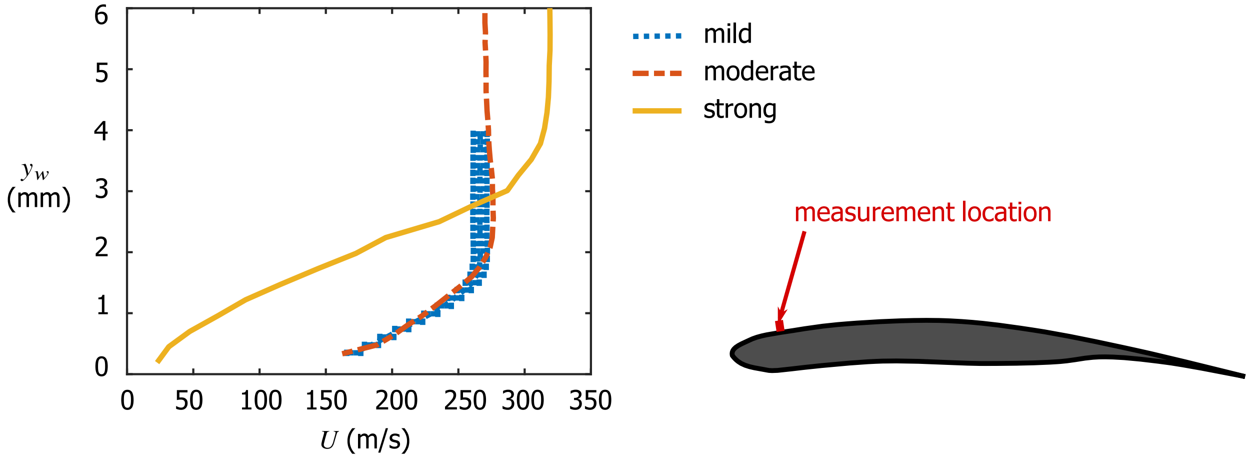

**Fig. 9** Boundary-layer profiles from LDV at $s = 0.14L_{\text{nac}}$ for a smooth surface at Mach 0.65. Error bars for the other data sets are excluded for clarity but are consistent with the mild windmilling case.

appear relatively large, some of the associated errors are systematic in nature and apply equally to all data points. For example, the same stagnation pressure measurement is used for all data points in a given series and so, whilst individual data values are associated with considerable relative uncertainties, the profile minimum can be considered to reliably indicate the stagnation point location. As the windmilling severity is increased, the stagnation point moves from about $s = -0.009L_{\mathrm{nac}}$ for mild windmilling to $s = -0.014L_{\mathrm{nac}}$ for strong windmilling, which corresponds to a movement into the intake by approximately $0.005L_{\mathrm{nac}}$ over the three cases.

The shifted stagnation point affects the flow field on the nacelle's external surface, as demonstrated by the surface pressure distribution in Fig. 6. All three cases show a supersonic region terminating in a normal shock which is roughly uniform across the span of the tunnel. The apparent spanwise pressure variation downstream of the shock is not physical but is instead an artefact of local surface temperature changes caused by thermally-conductive steel supports underneath the resin sleeve, which increase the local error in PSP measurements. As the windmilling severity increases, Fig. 6 shows that the supersonic region becomes larger. This effect is also evident in the surface pressure profile on the tunnel centre span (Fig. 7). This profile shows the shock wave moves downstream from $s/L_{\mathrm{nac}} = 0.04$ to $s/L_{\mathrm{nac}} = 0.07$ as the windmilling severity progresses from mild to strong. In addition, the Mach number immediately upstream of the shock increases from 1.25 to 1.55, corresponding to a normal shock wave with greater strength. The presence of the secondary shock identified in Fig. 4c is also captured in the isentropic Mach number distribution for strong windmilling (Fig. 7). Due to viscous smearing in the boundary layer and some secondary shock unsteadiness, the isentropic Mach number measured on the surface consists of a supersonic Mach number after the primary normal shock followed by a gradual reduction in Mach number to subsonic conditions by the secondary shock.

The variations in shock wave strength consequently impact the separation behaviour, as determined from oil-flow visualisation (Fig. 8). The position of the shock wave is evident in 8a from an accumulation of oil corresponding to a sudden reduction in shear stress. Nevertheless, the figure shows that during mild windmilling, the boundary layer remains attached across the majority of the tunnel span, except for a small region near the corners. For the moderate windmilling condition, Fig. 8b shows that the boundary layer is separated across much of the span of the tunnel which extends roughly $0.025L_{\mathrm{nac}}$ in the streamwise direction. In addition, noticeable corner separation has begun to develop near the tunnel sidewalls. Finally, under strong windmilling, there appears to be more substantial separation which is also more three-dimensional in nature. The streamwise separation length on the tunnel centreline has increased to 5% of the nacelle length and the corner separation has also grown in extent.

The effect of the development of separation on the external fan cowl boundary layer is clear from Fig. 9, which shows the velocity profile at $s/L_{\mathrm{nac}} = 0.145$. This figure shows that the boundary-layer thickness increases slightly from 1.8 mm to 2.1 mm as the flow state changes from attached (Fig. 8a) for mild windmilling to incipiently separated (Fig. 8b) for moderate windmilling. However, Fig. 9 shows that the boundary layer corresponding to Fig. 8c (strong windmilling) is significantly thicker (4.7 mm). This velocity distribution and boundary-layer parameters (Table 1) also

**Table 1 Integral parameters for boundary-layer profiles at $s = 0.14L_{\text{nac}}$ in Fig. 9 (smooth surface at Mach 0.65).**

| **windmilling severity** | boundary-layer thickness, $\delta$ (mm) | displacement thickness, $\delta_i^*$ (mm) | momentum thickness, $\theta_i$ (mm) | shape factor $H_i$ |
|---|---|---|---|---|
| **mild** | 1.79 | 0.36 | 0.24 | 1.51 |
| **moderate** | 2.08 | 0.41 | 0.27 | 1.50 |
| **strong** | 4.69 | 1.59 | 0.75 | 2.11 |

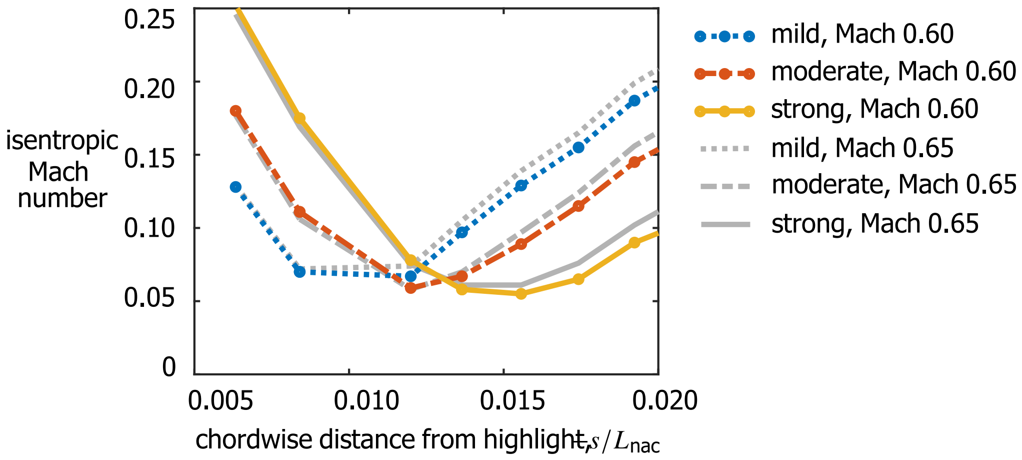

**Fig. 10 Isentropic Mach number around the stagnation point for a smooth surface at Mach 0.60 compared to Mach 0.65. Error bars are excluded for clarity but are consistent with those presented in Fig. 5.**

exhibit substantial deviations from an equilibrium flat plate, zero pressure-gradient turbulent profile [25], suggesting that the boundary layer is still recovering after reattachment. It is also worth noting that stronger windmilling severities correspond to increased freestream velocity. This observation can be attributed to: increased mass flow through the lower "external" flow channel; a thicker boundary layer producing an effective fan cowl profile which is less diffusive; and, for strong windmilling, local re-acceleration of the flow downstream of the primary shock.

### B. Effect of Mach number

When the incoming Mach number is reduced from 0.65 to 0.60 for the smooth surface, Fig. 10 shows that the position of the stagnation point remains essentially unchanged. However, Fig. 11 reveals that the supersonic region is substantially smaller than the Mach 0.65 case for all three windmilling scenarios. Indeed, the centreline pressure distribution indicates that the shock Mach number is roughly 10% lower than for $M_\infty = 0.65$ (Fig. 12). For mild windmilling, the shock has become so weak that it resembles a series of weak compression waves. These observations are consistent with the schlieren images in Fig. 13, which show a smaller supersonic region than Fig. 4. No shock wave at all is visible in Fig. 13a for the mild windmilling case. Meanwhile, the shock foot for the strong windmilling scenario (Fig. 13c) has transformed from a lambda-shock structure to a smeared normal shock, suggesting that the boundary layer now remains

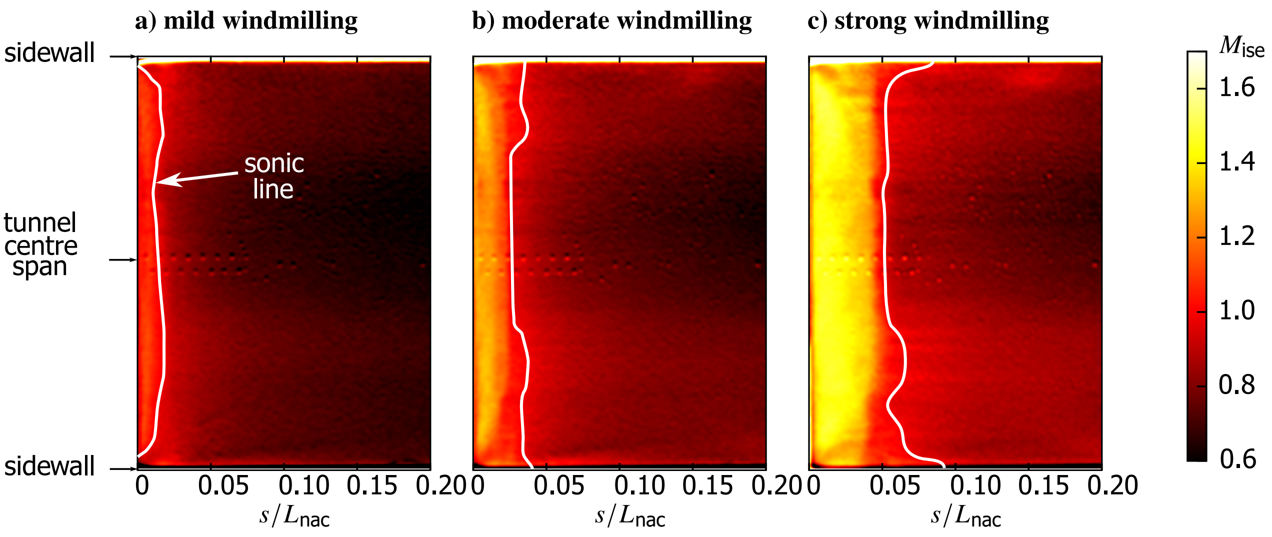

Fig. 11 Isentropic Mach number distribution from PSP on the external surface for a smooth surface at Mach 0.60.

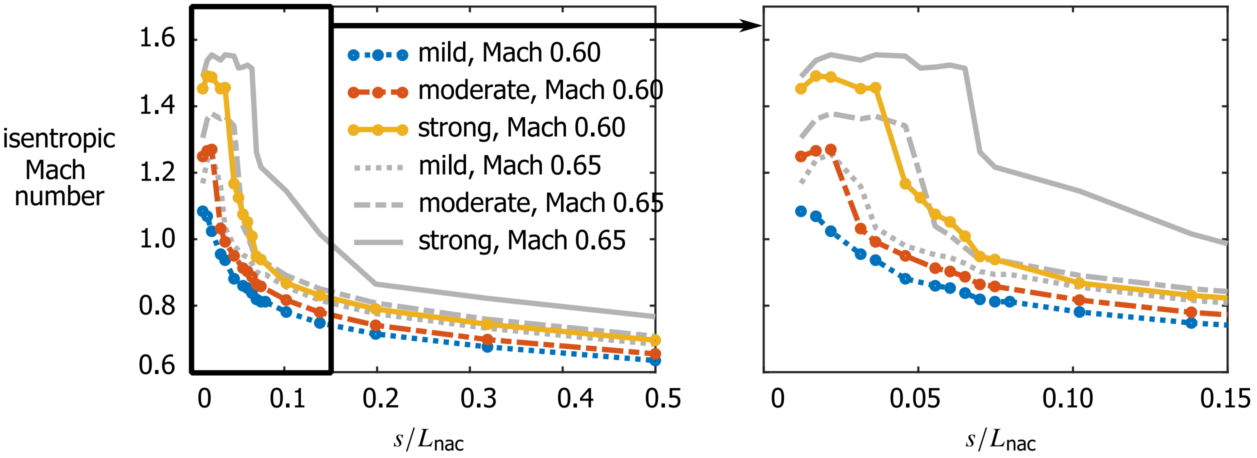

Fig. 12 Isentropic Mach number on the centre span of the external surface for a smooth surface at Mach 0.60 compared to Mach 0.65. Error bars are excluded for clarity but are consistent with those presented in Fig. 7.

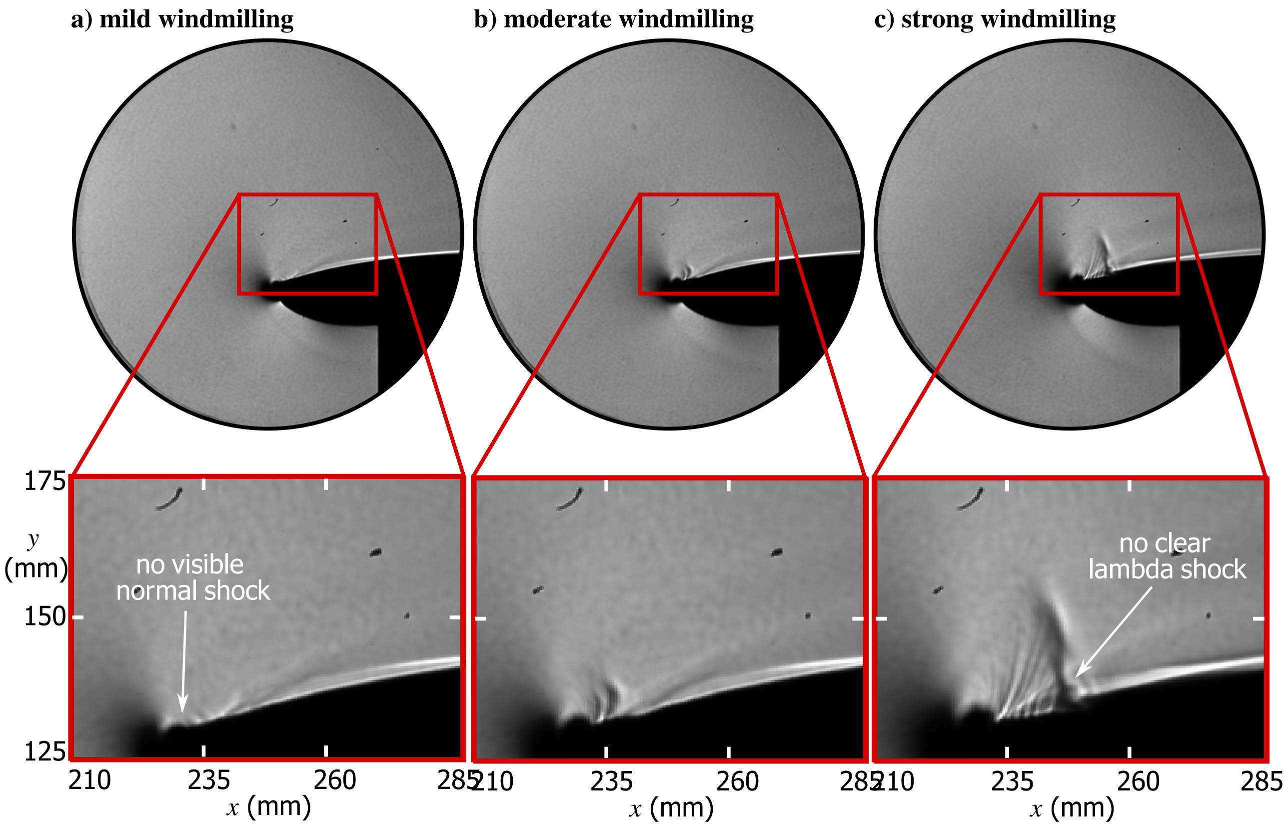
a) mild windmilling

b) moderate windmilling

c) strong windmilling

Fig. 13 Schlieren visualisation for a smooth surface at Mach 0.60.

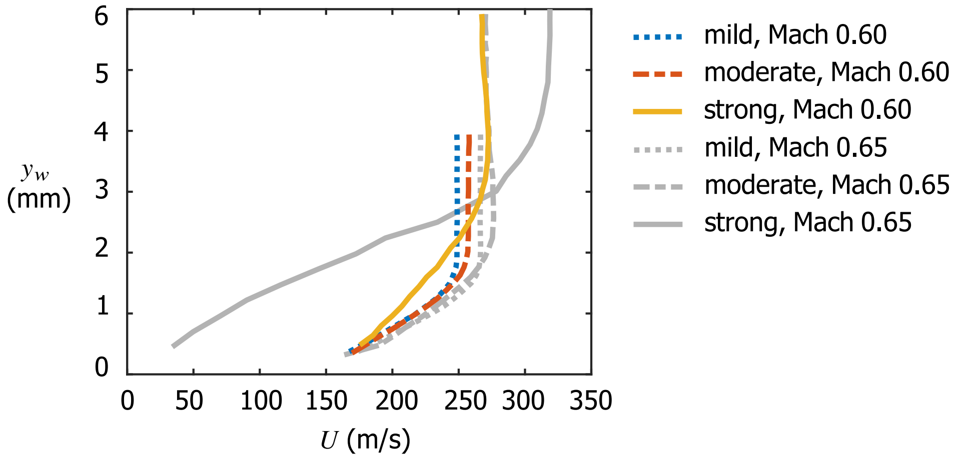

**Fig. 14 Boundary-layer profiles from LDV at $s = 0.14L_{\mathrm{nac}}$ for a smooth surface at Mach 0.60 compared to Mach 0.65. Error bars are excluded for clarity but are consistent with those presented in Fig. 9.**

**Table 2 Integral parameters for boundary-layer profiles at $s = 0.14L_{\mathrm{nac}}$ in Fig. 14 for a smooth surface at Mach 0.60 compared to Mach 0.65 (Table 1). Bracketed quantities represent the percentage difference to the Mach 0.65 values.**

| | **windmilling severity** | boundary-layer thickness, $\delta$ (mm) | displacement thickness, $\delta_i^*$ (mm) | momentum thickness, $\theta_i$ (mm) | shape factor $H_i$ |
|---|---|---|---|---|---|
| | **mild** | 1.79 | 0.36 | 0.24 | 1.51 |
| Mach 0.65 | **moderate** | 2.08 | 0.41 | 0.27 | 1.50 |
| | **strong** | 4.69 | 1.59 | 0.75 | 2.11 |
| | **mild** | 1.75 (–2%) | 0.33 (–8%) | 0.22 (–8%) | 1.49 (–1%) |
| Mach 0.60 | **moderate** | 1.94 (–7%) | 0.37 (–10%) | 0.25 (–7%) | 1.48 (–1%) |
| | **strong** | 3.26 (–30%) | 0.59 (–63%) | 0.41 (–45%) | 1.45 (–31%) |

attached.

Despite the mild windmilling case featuring a weaker shock wave at Mach 0.60 than at Mach 0.65, there is almost no difference in the corresponding downstream boundary-layer profiles in Fig. 14. Indeed, a comparison between Table 1 and Table 2 suggests that the boundary-layer parameters for mild windmilling all agree to within 10%. This is likely because, for this scenario, both the Mach 0.60 and Mach 0.65 cases correspond to the boundary-layer always having remained attached through the normal shock interaction. The boundary layer for moderate windmilling presents a small reduction in boundary-layer thickness at Mach 0.60 compared to the Mach 0.65 case but is otherwise similar in profile. The most pronounced change, however, is for strong windmilling, where the boundary layer at Mach 0.60 is about 30% thinner than at Mach 0.65 and has a much fuller profile, with the shape factor reduced by 30%. The reason for this is that the boundary layer in the Mach 0.60 case now remains attached through the interaction with the weaker shock, and thus the downstream boundary layer is thinner and has more momentum. This interpretation is consistent with the shock structure noted in schlieren images of the flow field (Fig. 13c).

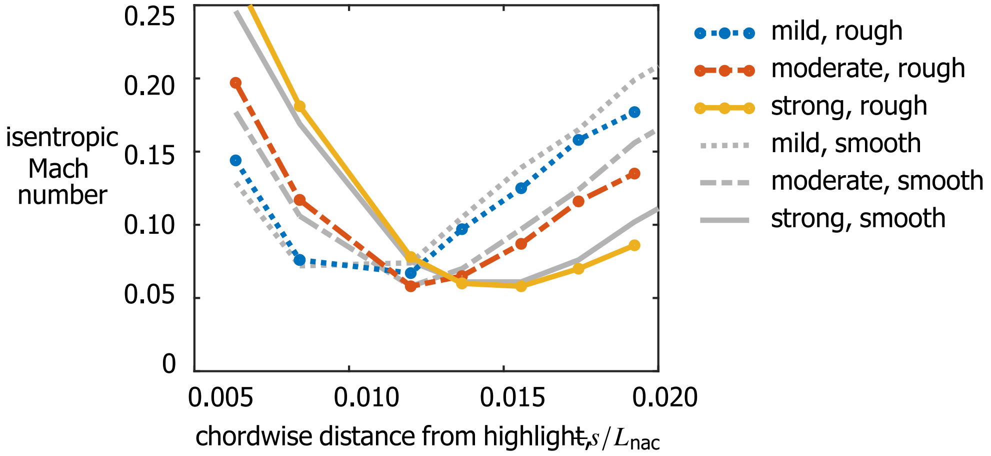

**Fig. 15 Isentropic Mach number around the stagnation point for a rough surface at Mach 0.65, compared to the smooth case. Error bars are excluded for clarity but are consistent with those presented in Fig. 5.**

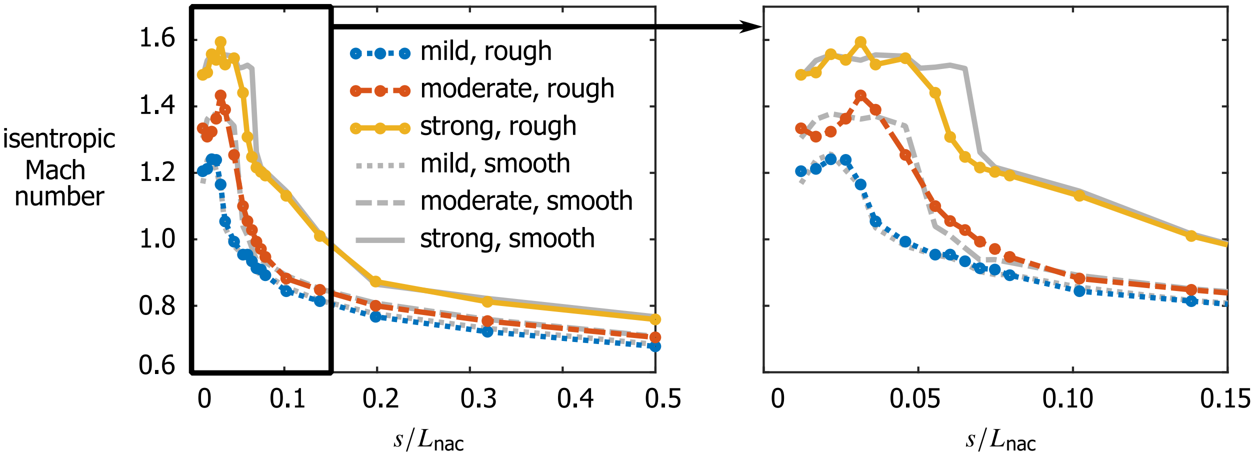

**Fig. 16 Isentropic Mach number on the centre span of the external surface for a rough surface at Mach 0.65, compared to the smooth case. Error bars are excluded for clarity but are consistent with those presented in Fig. 7.**

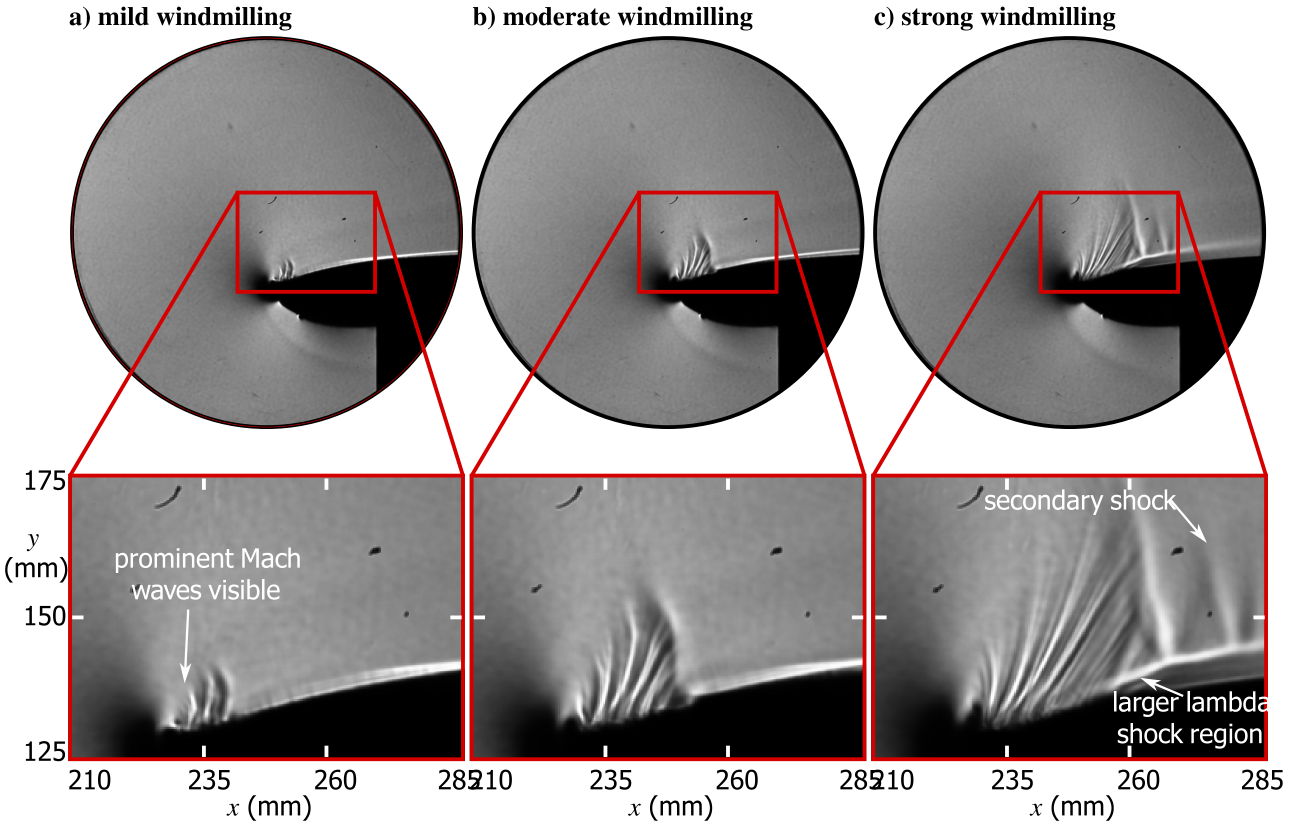
a) mild windmilling

b) moderate windmilling

c) strong windmilling

Fig. 17 Schlieren visualisation for a rough surface at Mach 0.65.

### C. Effect of surface roughness

For the nominal incoming Mach number of 0.65, the flow field is also analysed when the "smooth" surface with roughness height, 2.0 microns, is replaced by the "rough" surface, which has a roughness height of 16.1 microns. Figure 15 shows that, for a given windmilling severity, the stagnation point position is not affected by the change in surface roughness. Therefore, the effective engine mass-flow rate for each windmilling severity is similar between the smooth and rough cases, which means that differences in the flow field can be attributed to changes in the surface roughness. For all three windmilling severities, Fig. 16 shows that the shock strength also remains the same as for the smooth surface. Furthermore, the shock also has roughly the same position as the smooth case and the Mach number distributions are near-identical in the mild windmilling case. However, the moderate and strong windmilling scenarios exhibit some spikes in isentropic Mach number, with a less uniform Mach number in the supersonic region. The cause for these variations is not clear, but may be related to weak waves emitted from the roughness elements on the surface in the supersonic region. In addition, the moderate and strong windmilling cases exhibit a slightly more smeared shock wave with the rough surface than the smooth surface. For strong windmilling, the position of the shock wave has also moved slightly upstream by $0.01L_{\text{nac}}$ compared to the smooth case. For all three windmilling severities, the isentropic Mach number distribution downstream of the shock wave appears to be unaffected by the presence of surface roughness.

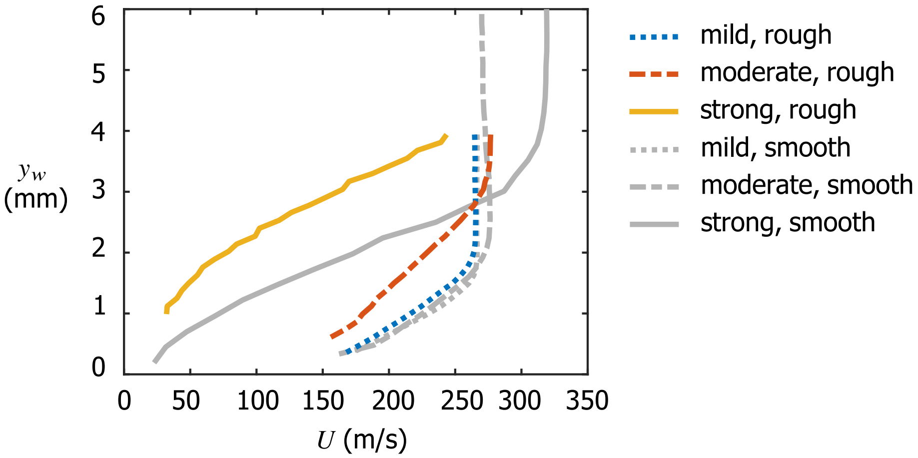

**Fig. 18 Boundary-layer profiles from LDV at $s = 0.14L_{\text{nac}}$ for a rough surface at Mach 0.65, compared to the smooth case. Error bars are excluded for clarity but are consistent with those presented in Fig. 9.**

These observations are consistent with the schlieren images of the flow field presented in Fig. 17. The size and the shape of the supersonic region in schlieren images is consistent with the smooth cases (Fig. 4). Notably, the size of the lambda-shock region in the moderate and strong windmilling flow fields is larger than the equivalent smooth images, consistent with the more smeared decrease in Mach number in Fig. 16. There are two other differences compared to the smooth cases. Firstly, the roughness elements cause a series of prominent, weak Mach waves to be emanated from the surface into the supersonic flow region. Secondly, the strong windmilling case in Fig. 17c features a larger, more prominent secondary shock following local re-acceleration of the post-shock, subsonic flow compared to the equivalent image with a smooth surface (Fig. 4c). This secondary shock is apparent not only in the instantaneous schlieren image presented but also in time-averaged representations of the flow field.

These differences can be attributed to the surface roughness reducing the momentum of the pre-shock boundary layer, increasing the height of the subsonic flow channel near the wall and enabling more effective upstream communication of the shock pressure rise. As a result, in the moderate and strong windmilling scenarios which feature boundary-layer separation, the lambda shock covers a larger region and the Mach number decrease is smeared over a greater distance. Furthermore, the lower-momentum boundary layer in the rough case is expected to grow thicker than for the smooth surface in response to the shock adverse pressure gradient. This boundary-layer response causes more pronounced streamline curvature in the external flow, which results in the re-acceleration of the post-shock flow to supersonic conditions and the associated secondary shock wave observed in Fig. 17c.

The changes to the shock–boundary-layer interaction also affect the post-shock boundary layer, which is shown in Fig. 18. For the cases where the free stream velocity is captured (mild and moderate windmilling), this velocity value is not affected by the presence of surface roughness, consistent with the observations of isentropic Mach number in Fig. 16. In the mild windmilling case, where the boundary layer remains attached, the velocity profile in Fig. 18 exhibits

**Table 3 Integral parameters for boundary-layer profiles at $s = 0.14L_{\text{nac}}$ in Fig. 18 for a rough surface at Mach 0.65 compared to the smooth case (Table 1). The entire profile is not captured for strong windmilling and so the boundary-layer parameters cannot be calculated. Bracketed quantities represent the percentage difference to the smooth case.**

| | **windmilling severity** | boundary-layer thickness, $\delta$ (mm) | displacement thickness, $\delta_i^*$ (mm) | momentum thickness, $\theta_i$ (mm) | shape factor $H_i$ |
|---|---|---|---|---|---|
| | **mild** | 1.79 | 0.36 | 0.24 | 1.51 |
| smooth | **moderate** | 2.08 | 0.41 | 0.27 | 1.50 |
| | **strong** | 4.69 | 1.59 | 0.75 | 2.11 |
| | **mild** | 2.12 (+18%) | 0.42 (+17%) | 0.28 (+17%) | 1.50 (−1%) |
| rough | **moderate** | 3.63 (+75%) | 0.82 (+100%) | 0.52 (+93%) | 1.59 (+6%) |
| | **strong** | - | - | - | - |

minimal changes. For example, the rough case features a boundary layer that is only 18% thicker than the smooth surface (Table 3). However, the separated scenarios (moderate and strong windmilling) display much thicker boundary layers for the rough surface compared to the smooth case. For example, during moderate windmilling, the boundary layer for the rough surface is 75% thicker than in the smooth case. Fig. 18 also shows that moderate and strong windmilling severities feature a significant reduction in near-wall momentum when the smooth wall is replaced by a rough surface. This behaviour is likely due to the lower-momentum boundary layer becoming much thicker in response to the shock pressure rise, along with the surface roughness inhibiting the recovery of the boundary layer to an equilibrium profile.

### D. Correlations of shock strength with other flow parameters

The data presented thus far describes how key flow variables (effective engine mass-flow rate, incoming Mach number and surface roughness) affect the response of the external fan cowl boundary layer and thus impact nacelle aerodynamic performance. In addition, the measurements provide an opportunity to obtain insight into the mechanisms governing the shock-induced boundary-layer separation. For example, Figure 19 indicates that the strength of the shock (i.e. the supersonic Mach number immediately ahead of the shock wave) has a profound influence on the properties of the downstream boundary layer.

For shocks weaker than Mach 1.4, where the boundary layer remains attached, the boundary-layer thickness, the displacement thickness, and the shape factor are all relatively insensitive to the strength of the shock. However, for shocks which are strong enough to separate the boundary layer ($M_{\text{shock}} > 1.4$) an increase in shock strength corresponds to a considerable increase in boundary-layer thickness, displacement thickness and shape factor, which is consistent with a more severe separation. For example, at the measurement location 14% along the nacelle chord, there is a four-fold increase in displacement thickness between the weakest and strongest shocks in the current study. Therefore, Fig. 19 demonstrates that the shock strength is a key parameter governing the onset and scale of flow separation.

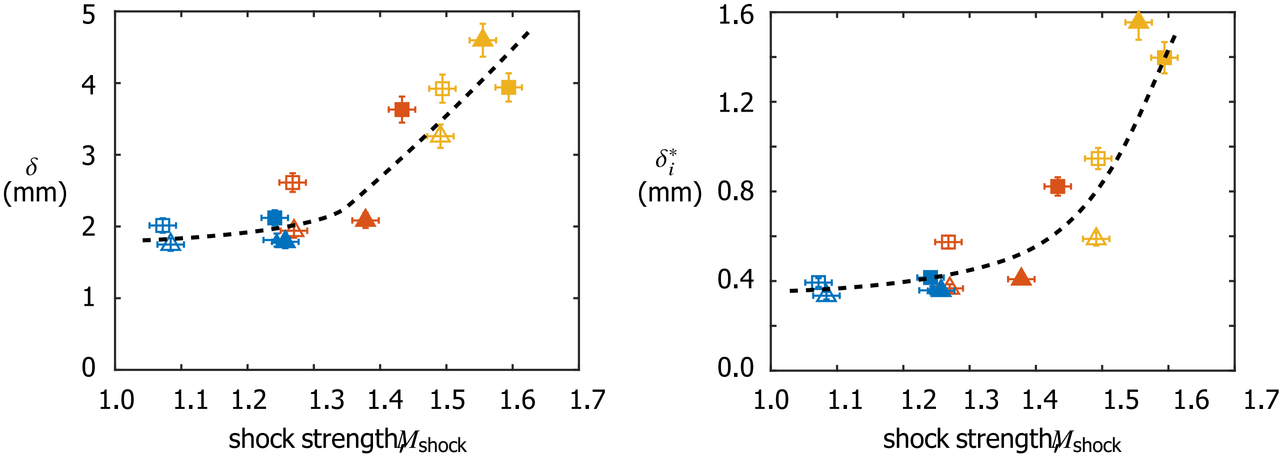
a) boundary-layer thickness

b) displacement thickness

c) shape factor

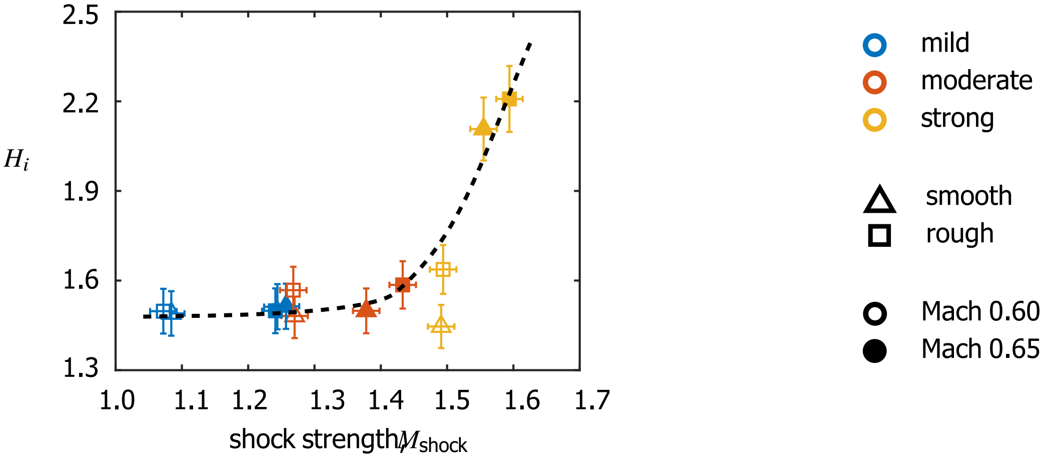

**Fig. 19** **Correlation between measured boundary-layer parameters and shock strength.**

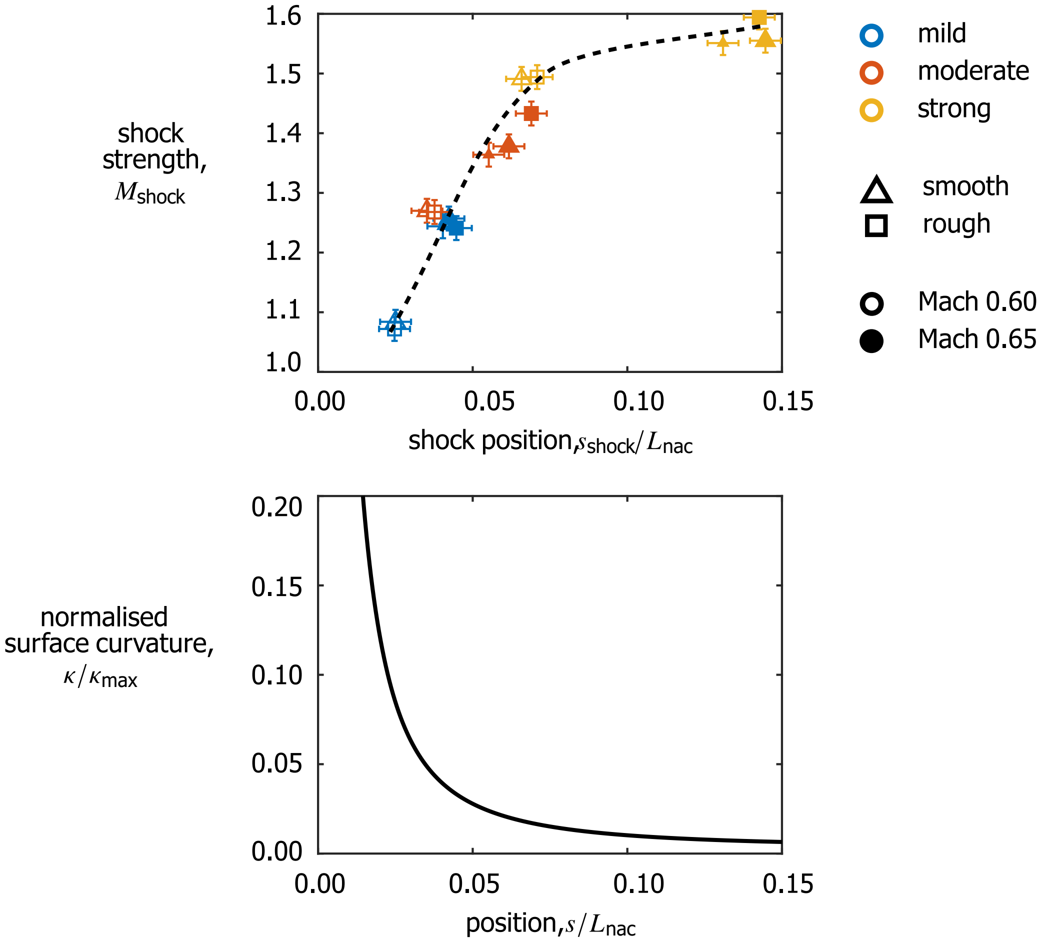

**Fig. 20** Correlation between shock strength and shock position, including normalised local surface curvature.

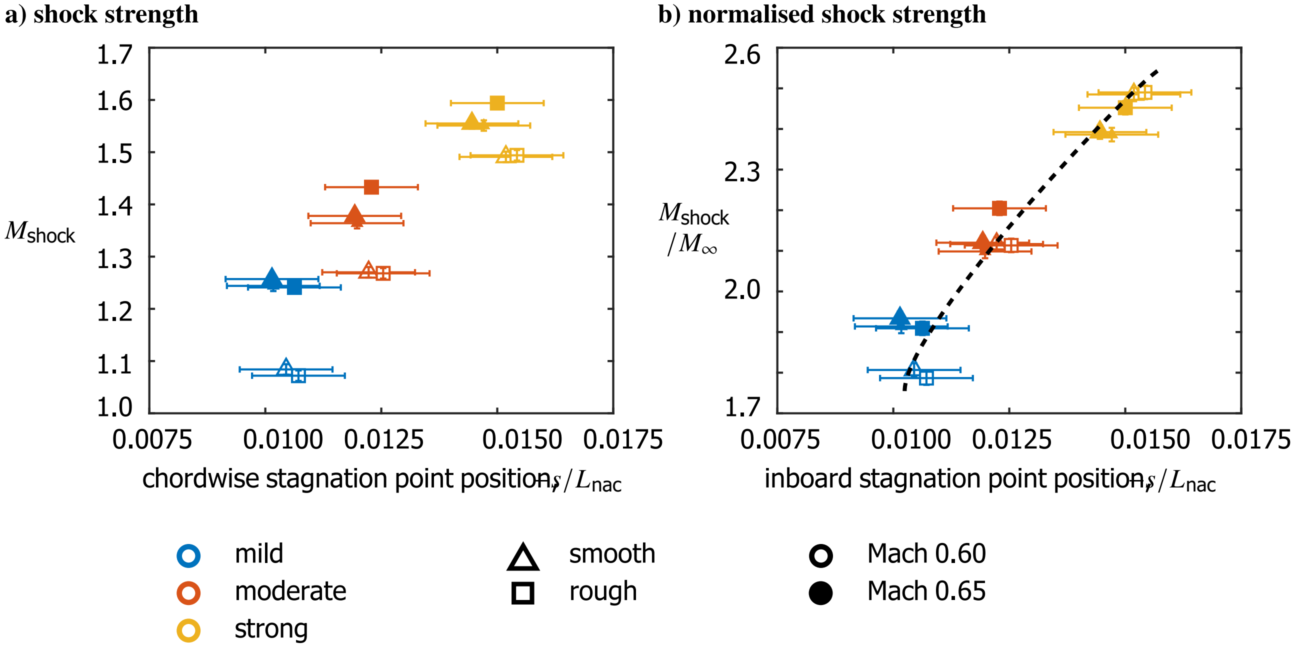

**Fig. 21 Correlation between stagnation point location and shock strength.**

Due to the importance of shock strength on the flow field, it is helpful to consider the correlation between shock strength and the shock position, i.e. the location where $M_{\text{ise}} = 1$. Figure 20 reveals that there is a close relationship between these two parameters. Indeed, a more downstream shock wave has experienced greater acceleration around the nacelle lip and thus features a higher Mach number. Note that, downstream of $0.08L_{\text{nac}}$, the curvature of the nacelle geometry is almost zero and thus, for shocks in this region (typically those in excess of Mach 1.5), even substantial changes in shock position are likely to cause only a small change in shock strength. This observation provides an explanation for why the strong windmilling case in Fig. 12 exhibits a relatively small change in shock strength between Mach 0.60 and Mach 0.65 despite a considerable change in shock position.

Note that the correlation between shock strength and shock position affects the interpretation of the boundary-layer parameters in Fig. 19. Since the boundary layer is known to recover most quickly downstream of the shock wave [23], a stronger shock wave might result in a thicker measured boundary layer for two reasons: firstly, the stronger shock wave has caused a more severe separation; secondly, a stronger shock wave is more downstream and therefore the boundary layer has a shorter recovery distance prior to the measurement station. Whilst it is difficult to decouple the two effects, the Appendix includes boundary-layer data from stations at different post-shock distances, which suggests that recovery distances of the boundary layer are on the order of $0.12L_{\text{nac}}$.

In order to understand the factors which determine the strength of the shock wave, Fig. 21 considers the correlation between the stagnation point location and the shock strength. Fig. 21a indicates that a more downstream stagnation point (i.e. further inside the intake) generally corresponds to a stronger shock wave, but there is considerable scatter.

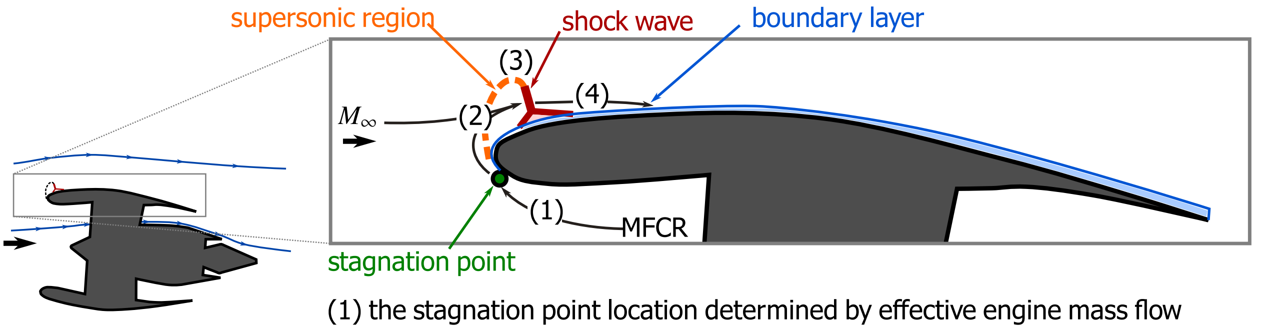

(1) the stagnation point location determined by effective engine mass flow
(2) shock strength depends on stagnation point position and incoming Mach number
(3) a stronger shock tends to be located further downstream
(4) an increased shock strength results in deteriorated boundary layer

**Fig. 22 Conceptual model summarising relationships between key flow parameters in the diversion windmilling flow field.**

When the shock Mach number is normalised by the entry Mach number in Fig. 21b, an excellent collapse of the data is obtained. Thus, both the stagnation point location and the incoming Mach number influence the shock strength. Physically, the incoming Mach number defines the starting condition whilst the stagnation point location determines the streamwise distance over which acceleration occurs around the leading edge.

## IV. Conclusions

The development of ultra-high bypass ratio engines will benefit from the drag reduction opportunities of compact nacelles, and so it is becoming increasingly important to understand external fan cowl separation sensitivity under off-design conditions like diversion windmilling. These conditions are defined by a reduced flight Mach number and decreased engine mass-flow rate compared to nominal cruise values. This paper presents experiments performed in a transonic, quasi-two-dimensional wind tunnel rig, which is carefully designed to replicate the flow physics from a full-scale nacelle. The current investigation focuses on the effects of the effective engine mass-flow rate (or "windmilling severity"), the incoming freestream Mach number, and the surface roughness. The observed effects can be explained by the conceptual model derived from the measurements, which is summarised in Fig. 22.

For a given nacelle geometry and incidence angle, the strength of the normal shock wave on the external fan cowl surface is determined primarily by the stagnation point position and the incoming Mach number. As the equivalent engine mass-flow rate is reduced (i.e. stronger windmilling), there is a smaller capture streamtube and thus the stagnation point sits further downstream inside the intake. The flow is therefore accelerated more severely around the leading edge, resulting in a supersonic region with increased Mach number on the external surface. The terminating normal shock therefore becomes stronger and moves towards the trailing edge. Once the shock strength exceeds Mach 1.4, the onset of shock-induced boundary-layer separation is observed and the separation extent grows as the "windmilling severity" is further increased. The onset of shock-induced separation causes the downstream boundary layer at roughly 15% of the chord length to thicken by a factor of 2.6 for strong windmilling compared to mild windmilling.

When the incoming Mach number is reduced from 0.65 to 0.60, the flow field becomes considerably more benign. The supersonic region features Mach numbers approximately 10% lower than the nominal Mach 0.65 condition. Thus, the normal shock is correspondingly weaker and located further upstream. No substantial boundary-layer separation is detected over the engine mass-flow range considered. As a result, the strong windmilling case at Mach 0.60 exhibits a boundary layer which contains greater near-wall momentum and which is 30% thinner than at $M_\infty = 0.65$, where well-developed separation is observed.

When the roughness height on the external fan cowl surface is increased from 2.0 microns to 16.1 microns (corresponding to an increase from 6 microns to 50 microns at full scale) the stagnation point, shock strength and shock position are mostly unaffected during tests carried out at Mach 0.65. For mild windmilling, which features an attached shock–boundary-layer interaction, the downstream boundary layer is unchanged by the increased surface roughness. However, the moderate and strong windmilling cases, where the boundary layer tends to separate, exhibit a larger lambda-shock region for the rough surface, likely due to more effective upstream transmission of pressure information. As a result, the separation extent is larger and the post-shock boundary layer is 75% thicker than the smooth surface.

The experiments provide insight into the mechanisms defining external fan cowl separation during diversion windmilling. Nevertheless, a number of open questions remain. For example, whilst it has been established that the position (and thus the strength) of the normal shock is determined by the incoming Mach number and the stagnation point location, it is not clear what role (if any) is played by the trailing-edge Mach number. Furthermore, the collected measurements constitute a valuable validation data set and so comparisons of experimental data against equivalent computations will enable evaluation of their capabilities and limitations in predicting separation during diversion windmilling scenarios, as required to guide the design of UHBPR nacelles.

## Funding Sources

This project has received funding from the Clean Sky 2 Joint Undertaking (JU) under grant agreement No 101007598. The JU receives support from the European Union's Horizon 2020 research and innovation programme and the Clean Sky 2 JU members other than the Union. The wind tunnel forms part of the UK National Wind Tunnel Facility, whose support is gratefully acknowledged.

## Acknowledgements

The authors would like to thank D. Martin, A. Luckett and C. Costello for operating the blow-down wind tunnel. The authors are also grateful to A. Dennis for assistance with profilometer measurements and to N. Atkins and W. Davis for loan and assistance with the operation of the infrared thermography camera.

# References

[1] Tejero, F., Robinson, M., MacManus, D., and Sheaf, C., "Multi-objective optimisation of short nacelles for high bypass ratio engines," *Aerospace Science and Technology*, Vol. 91, 2019, pp. 410–421. https://doi.org/10.1016/j.ast.2019.02.014.

[2] Zachos, P., "Modelling and analysis of turbofan engines under windmilling conditions," *Journal of Propulsion and Power*, Vol. 29, No. 4, 2013, pp. 882–890. https://doi.org/10.2514/1.b34729.

[3] European Commission, "FlightPath 2050: Europe's vision for aviation," Tech. Rep. EUR 098 EN, Publications Office of the European Union, 2011. https://doi.org/10.2777/50266.

[4] Magrini, A., Benini, E., Yao, H.-D., Postma, J., and Sheaf, C., "A review of installation effects of ultra-high bypass ratio engines," *Progress in Aerospace Sciences*, Vol. 119, 2020, p. 100680. https://doi.org/10.1016/j.paerosci.2020.100680.

[5] Tejero, F., MacManus, D., Matesanz García, J., Swarthout, A., and Sheaf, C., "Towards the design and optimisation of future compact aero-engines: intake/fancowl trade-off investigation," *International Journal of Numerical Methods for Heat & Fluid Flow*, Vol. 33, No. 4, 2023, pp. 1319–1335. https://doi.org/10.1108/hff-06-2022-0366.

[6] Hoelmer, W., Younghans, J., and Raynal, J., "Effect of Reynolds number on upper cowl flow separation," *Journal of Aircraft*, Vol. 24, No. 3, 1987, pp. 161–169. https://doi.org/10.2514/3.45411.

[7] Mitchell, D., and Carr, A., "Estimation of Windmill Drag and Airflow of Turbojet and Turbofan Engines," Tech. Rep. ESDU-81009, Engineering Sciences Data Unit, 1984.

[8] Cao, T., Vadlamani, N., Tucker, P., Smith, A., Slaby, M., and Sheaf, C., "Fan–intake interaction under high incidence," *Journal of Engineering for Gas Turbines and Power*, Vol. 139, No. 4, 2017, p. 041204. https://doi.org/10.1115/1.4034701.

[9] Boscagli, L., Christie, R., MacManus, D., and Piovesan, T., "Aerodynamics of a short intake in crosswind," *Aerospace Science and Technology*, Vol. 129, 2022, p. 107826. https://doi.org/10.1016/j.ast.2022.107826.

[10] Wakelam, C., Hynes, T., Hodson, H., Evans, S., and Chanez, P., "Separation control for aero engine intakes, part 2: high-speed investigations," *Journal of Propulsion and Power*, Vol. 28, No. 4, 2012, pp. 766–772. https://doi.org/10.2514/1.59224.

[11] Boscagli, L., MacManus, D., Christie, R., and Sheaf, C., "Effect of unsteady fan-intake interaction on short intake design," *Journal of Engineering for Gas Turbines and Power*, Vol. 146, 2024, pp. 031008–1. https://doi.org/10.1115/1.4063768.

[12] Boscagli, L., MacManus, D., Tejero, F., Sabnis, K., Babinsky, H., and Sheaf, C., "Characteristics of shock-induced boundary-layer separation on nacelles under windmilling diversion conditions," *AIAA Journal*, Vol. 62, No. 1, 2024, pp. 79–91. https://doi.org/doi.org/10.2514/1.j063209.

[13] Kalsi, H., and Tucker, P., "Numerical modelling of shock wave boundary layer interactions in aero-engine intakes at incidence," *Proceedings of ASME Turbo Expo 2018 Turbomachinery Technical Conference and Exposition*, Vol. 50985, GT2018-75872, American Society of Mechanical Engineers, 2018. https://doi.org/10.1115/gt2018-75872.

[14] Sabnis, K., Babinsky, H., Boscagli, L., Swarthout, A., Tejero, F., MacManus, D., and Sheaf, C., "A wind tunnel rig to study the external fan cowl separation experienced by compact nacelles in windmilling scenarios," *AIAA Scitech 2023 Forum*, 2023-1942. https://doi.org/10.2514/6.2023-1942.

[15] Boscagli, L., Tejero, F., Swarthout, A., MacManus, D., Sabnis, K., Babinsky, H., and Sheaf, C., "Design of a quasi-2D rig configuration to assess nacelle aerodynamics under windmilling conditions," *AIAA Aviation 2023 Forum*, 2023-3392. https://doi.org/10.2514/6.2023-3392.

[16] Swarthout, A., MacManus, D., Tejero, F., Matesanz Garcia, J., Boscagli, L., and Sheaf, C., "A comparative assessment of multi-objective optimisation methodologies for aero-engine nacelles," *33rd Congress of the International Council of the Aeronautical Sciences*, 2022, Paper ICAS2022-0162.

[17] Davis, W., and Atkins, N., "Infrared thermography techniques for boundary layer state visualisation," *Experiments in Fluids*, Vol. 65, No. 6, 2024, pp. 1–17. https://doi.org/10.1007/s00348-024-03827-8.

[18] Gregory, J., Asai, K., Kameda, M., Liu, T., and Sullivan, J., "A review of pressure-sensitive paint for high-speed and unsteady aerodynamics. Proceedings of the Institution of Mechanical Engineers," *Part G: Journal of Aerospace Engineering*, Vol. 222, No. 2, 2008, pp. 249–290. https://doi.org/10.1243/09544100jaero243.

[19] Colliss, S., Babinsky, H., Nübler, K., and Lutz, T., "Vortical structures on three-dimensional shock control bumps," *AIAA Journal*, Vol. 54, No. 8, 2016, pp. 2338–2350. https://doi.org/10.2514/1.j054669.

[20] Squire, L., "The motion of a thin oil sheet under the steady boundary layer on a body," *Journal of Fluid Mechanics*, Vol. 11, No. 2, 1961, pp. 161–179. https://doi.org/10.1017/s0022112061000445.

[21] Sun, C., and Childs, M., "A modified wall wake velocity profile for turbulent compressible boundary layers," *Journal of Aircraft*, Vol. 10, No. 6, 1973, pp. 381–383. https://doi.org/10.2514/3.44376.

[22] Musker, A., "Explicit expression for the smooth wall velocity distribution in a turbulent boundary layer," *AIAA Journal*, Vol. 17, No. 6, 1979, pp. 655–657. https://doi.org/10.2514/3.61193.

[23] Babinsky, H., and Harvey, J., *Shock wave–boundary-layer interactions*, Cambridge Aerospace Series, Vol. 32, Cambridge University Press, 2011. https://doi.org/10.1017/cbo9780511842757.

[24] Titchener, N., Colliss, S., and Babinsky, H., "On the calculation of boundary-layer parameters from discrete data," *Experiments in Fluids*, Vol. 56, No. 8, 2015, p. 159. https://doi.org/10.1007/s00348-015-2024-5.

[25] Anderson, B., Tinapple, J., and Surber, L., "Optimal control of shock wave turbulent boundary layer interactions using micro-array actuation," *3rd AIAA Flow Control Conference*, 2006-3197. https://doi.org/10.2514/6.2006-3197.

## Appendix: Post-Shock Boundary-Layer Recovery

The boundary-layer profiles and associated parameters which are presented in the main paper are all collected at $s = 0.14L_{\text{nac}}$. However additional measurements collected at $s = 0.04L_{\text{nac}}$, $0.07L_{\text{nac}}$ and $0.11L_{\text{nac}}$ enable the boundary-layer parameters to be plotted as a function of post-shock distance. Figure 23 indicates that the boundary-layer parameters immediately downstream of the shock wave exhibits considerable scatter, since the response of the boundary layer is a function of shock strength. Nevertheless, approximately $0.12L_{\text{nac}}$ downstream of the shock, the boundary layer in all cases recovers to roughly the same equilibrium state.

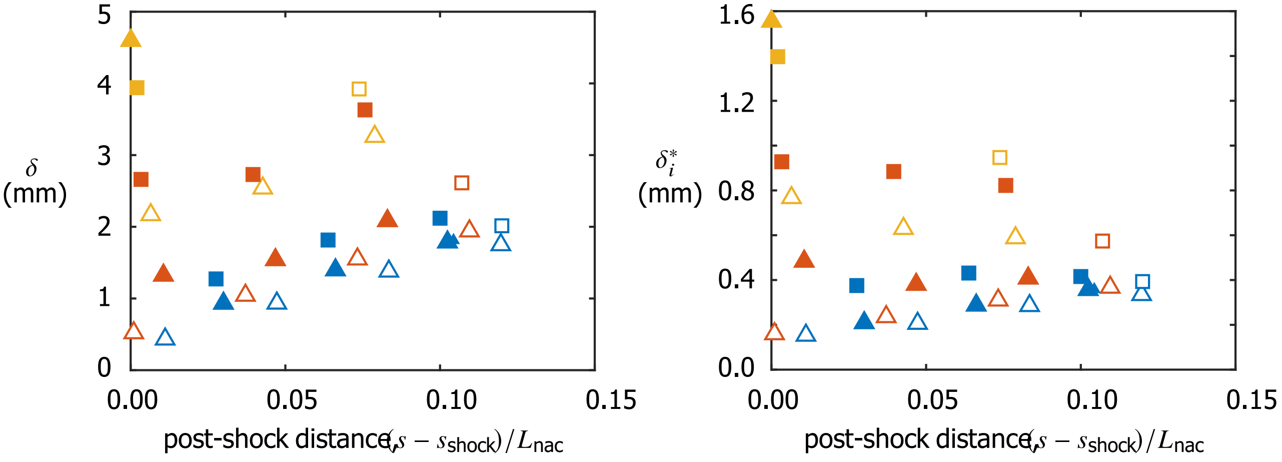
a) boundary-layer thickness

b) displacement thickness

c) shape factor

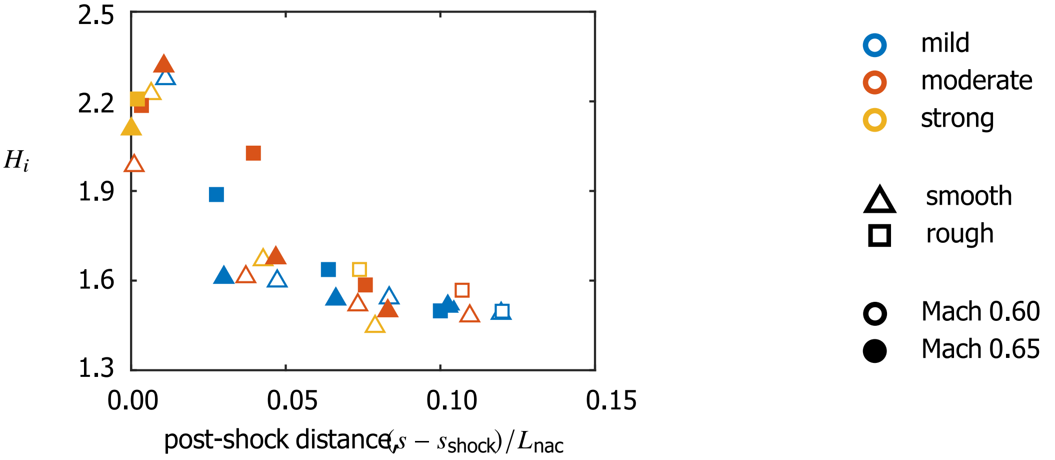

Fig. 23 **Measured boundary-layer parameters as a function of post-shock distance.**

# Shock-induced fan cowl separation during aeroengine windmilling at diversion from cruise

Sabnis, Kshitij

2025-03

Sabnis K, Babinsky H, Boscagli L, et al., (2025) Shock-induced fan cowl separation during aeroengine windmilling at diversion from cruise. AIAA Journal, Volume 63, Issue 3 March 2025, pp. 825-838

https://doi.org/10.2514/1.j064521